Forschungszentrum Karlsruhe
Technik und Umwelt

Wissenschaftliche Berichte
FZKA 6378

Strength and Toughness Test Devices with Opposite Roller Loading

T. Fett, D. Munz, G. Thun
Institut für Materialforschung

März 2000

FORSCHUNGSZENTRUM KARLSRUHE

Technik und Umwelt

Wissenschaftliche Berichte

FZKA 6378

Strength and toughness test devices with opposite roller loading

T. Fett, D. Munz, G. Thun

Institut für Materialforschung

Forschungszentrum Karlsruhe GmbH, Karlsruhe

2000

Als Manuskript gedruckt

Forschungszentrum Karlsruhe GmbH
Postfach 3640, 76021 Karlsruhe

Mitglied der Hermann von Helmholtz-Gemeinschaft
Deutscher Forschungszentren (HGF)

ISSN 0947-8620

Strength and toughness test devices with opposite roller loading

Abstract:

Bars loaded by opposite concentrated forces via rollers are appropriate test specimens for the determination of the fracture toughness K_{Ic}, the crack resistance curve (R-curve), and strength under contact loading located in the second quadrant ($\sigma_1 > 0$, $\sigma_2 < 0$) of the biaxial failure diagram. In this report stress solutions are provided for the proposed strength specimens. For the fracture mechanics specimens containing edge cracks, stress intensity factor solutions are given in the form of figures and tables.

As practical applications of the specimens proposed, the strengths for two aluminas and for a commercial PZT ceramic (PIC 151, PI-Ceramic) are reported. In addition, crack resistance measurements are carried out.

Testapparaturen zur Bestimmung der Rißzähigkeit und Festigkeit von Keramikstäben durch Rollenbelastung

Kurzfassung:

Es werden Tests zur Bestimmung der Rißzähigkeit K_{Ic}, der Rißwiderstandskurve (R-Kurve) und zur Ermittlung der Festigkeit unter Kontaktbelastung mit Spannungen im Bereich ($\sigma_1 > 0$, $\sigma_2 < 0$) des Mehrachsigkeits-Diagramms vorgeschlagen. Im vorliegenden Bericht werden die Spannungsverteilungen bei symmetrischer Kontaktbelastung berechnet. Sie erlauben die Bestimmung der mehrachsigen Festigkeit unter Kontaktlast. Für bruchmechanische Proben mit durchgehenden Oberflächenrissen ("edge cracks") werden die Lösungen für den Spannungsintensitätsfaktor in Diagrammen und Tabellen angegeben.

Als praktische Anwendung der vorgeschlagenen Versuche werden die Festigkeiten zweier Aluminiumoxide und einer kommerziellen Piezo-Keramik gemessen. Zusätzlich werden Messungen des Rißwiderstands durchgeführt.

Contents

1 Introduction

The determination of fracture toughness needs test specimens with sharp cracks. In metals cracks are introduced as fatigue cracks starting from a notch. In ceramics the creation of cracks is more difficult. For coarse-grained ceramic materials it is sufficient to use narrow notches introduced by a saw cut. For notch preparation mostly thin copper wheels coated with diamond powder are used. Notches of about 50-60 μm width can be produced with this technique. A procedure proposed by Nishida et al. [1] allows to introduce notches with notch root radii in the range of 1-10 μm. In the first step a conventional saw cut is introduced. Then a sharp V-shaped notch is produced by using a razor blade and diamond paste. For fine-grained materials with mean grain size of less than 1μm the application of sharp cracks is necessary. The generation of an ideal sharp crack in a test specimen is rather difficult.

Figure 1 shows the bridge method [2][3]. A starter crack (e.g. a Vickers indentation) is introduced into the specimen surface. Then the specimen is placed on a plane support and loaded with a bridge. A macroscopic crack starts from the indentation and extends over the whole specimen thickness. In principle, this arrangement may be used not only for crack generation but also for the determination of R-curves. Unfortunately, the friction conditions and the pressure distribution at the contact area between the bridge ends and the upper specimen surface are not well defined. The same holds for the contact area between the specimen and the supporting structure.

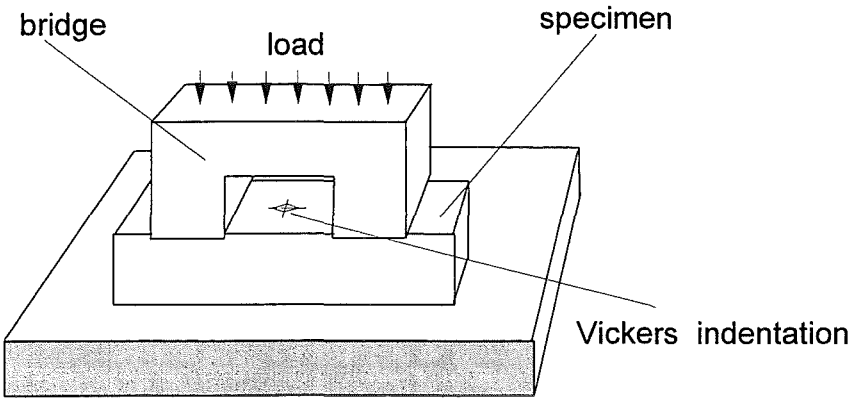

Fig. 1 Crack generation with the bridge method [2][3].

As a modification of the bridge method, a loading via two free rollers of short distance d (see Fig. 2) is proposed. A rectangular bar of width W and thickness t is bedded on a rigid support. The procedure is similar to that of the conventional bridge method. Due to the free rollers, it is easier to ensure line contacts, whereas the bridge method with flat stamps needs the contact over an extended area.

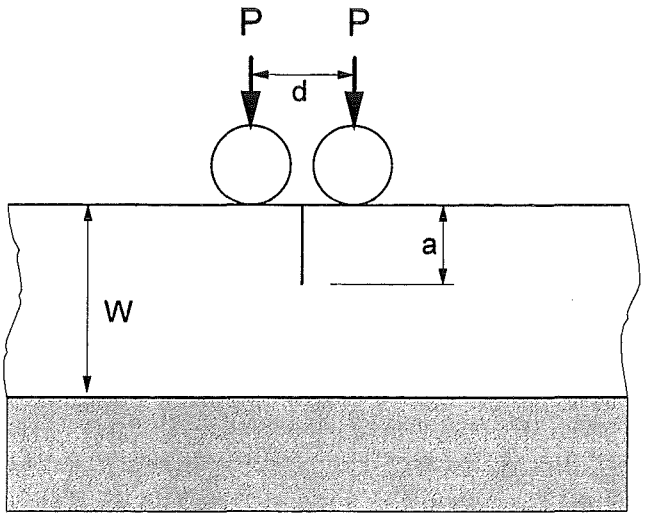

Fig. 2 Cracked specimen loaded with two rollers and supported on a rigid plate (thickness t).

A third proposed test device avoids the remaining uncertainties in supporting (full contact over the supporting area) by a symmetrical load application via four symmetrically arranged rollers (Fig. 3).

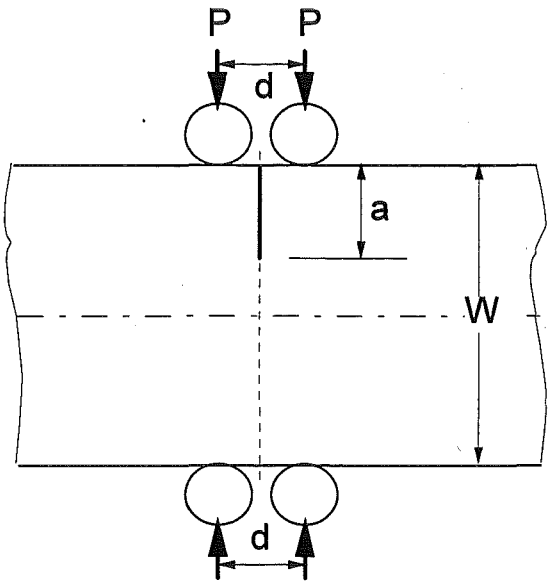

Fig. 3 Controlled fracture test device with load application via four symmetrical rollers.

For a further application of diametral roller loadings a strength test under contact loading is proposed as illustrated in Fig. 4. In this type of test a biaxial stress is generated in the cross section between the two opposite loading rollers, which allows to determine strength in the second quadrant of a biaxial failure diagram with the principal stresses $\sigma_1 > 0$, $\sigma_2 < 0$. The test can be carried out with simple bending bars ($3 \times 4 \times 45$ mm^3) or fragments of shorter length. Strength determination in such a test may compete with the well-known Brazilian Disk test (see e.g. [4] [5]) which needs special specimens and test equipment.

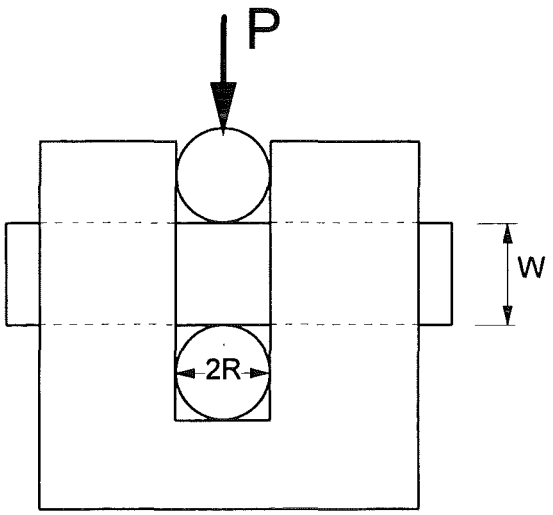

Fig. 4 A contact strength test with different signs of the principal stresses.

In the following computations the special case of an infinitely long parallel strip is considered. This case is fulfilled by a length-to-width ratio of $2L/W = 45$ mm/4 mm. Sometimes it may be of advantage to test specimens of shorter length, e.g. fragments of bars. Therefore, the influence of a short specimen length on the stress state is addressed in the Appendix.

2 Computation of stresses for opposite loads

2.1 Stresses caused by a single pair of concentrated opposite line forces

The stresses in the strip of width $2H = W$ (Fig. 4) and thickness t, loaded by opposite concentrated forces P, have been computed by Filon [6]. With the geometric data shown in Fig. 5 the stresses can be expressed by

$$\sigma_x = -\frac{2P}{\pi H t}\int_0^\infty \frac{\sinh u - u\cosh u}{\sinh 2u + 2u}\cos\frac{ux}{H}\cosh\frac{uy}{H}\,du -$$

$$-\frac{2P}{\pi H t}\int_0^\infty \frac{uy}{H}\frac{\sinh u}{\sinh 2u + 2u}\cos\frac{ux}{H}\sinh\frac{uy}{H}\,du \qquad (1)$$

$$\sigma_y = -\frac{2P}{\pi H t}\int_0^\infty \frac{\sinh u + u\cosh u}{\sinh 2u + 2u}\cos\frac{ux}{H}\cosh\frac{uy}{H}\,du$$

$$+\frac{2P}{\pi H t}\int_0^\infty \frac{uy}{H}\frac{\sinh u}{\sinh 2u + 2u}\cos\frac{ux}{H}\sinh\frac{uy}{H}\,du \qquad (2)$$

$$\tau_{xy} = \frac{2P}{\pi H t}\int_0^\infty \frac{u\cosh u}{\sinh 2u + 2u}\sin\frac{ux}{H}\sinh\frac{uy}{H}\,du$$

$$-\frac{2P}{\pi H t}\int_0^\infty \frac{uy}{H}\frac{\sinh u}{\sinh 2u + 2u}\sin\frac{ux}{H}\cosh\frac{uy}{H}\,du \qquad (3)$$

The stresses are plotted in Figs. 6-8 and normalised to

$$\sigma^* = \frac{P}{Ht} \qquad (4)$$

The stress component σ_x is represented in Fig. 6. Close to the surface tensile stresses occur, which change to compression and reach tension again in the specimen centre. The shear stress τ_{xy}, plotted in Fig. 7, is antisymmetric with respect to the centre line (y=0). Figure 8 illustrates the stress component σ_y.

Instead of the representation by the stress components σ_x, σ_y and τ_{xy}, the stress state may also be described by the principal stresses and the maximum shear stresses (see Appendix).

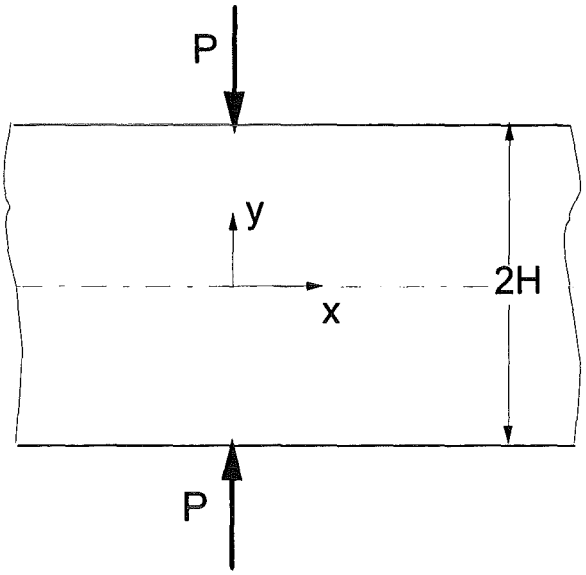

Fig. 5 Infinitely long strip loaded by a pair of opposite concentrated forces.

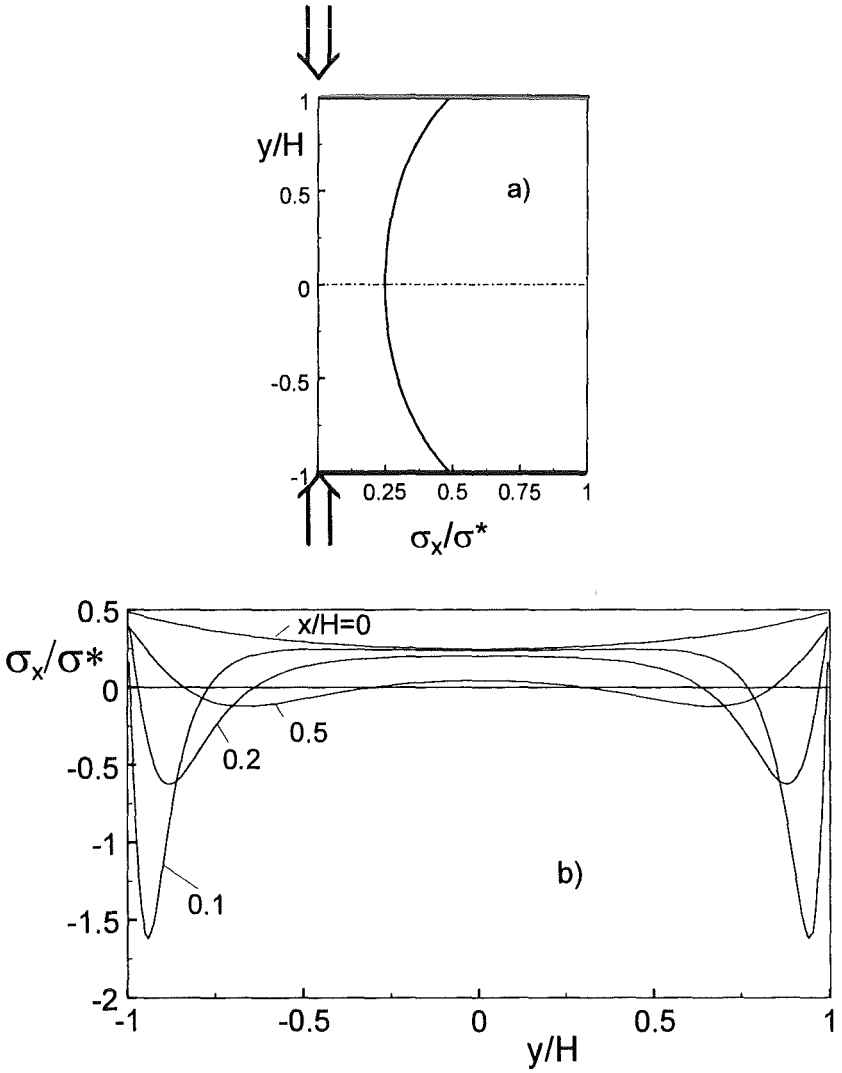

Fig. 6 Stress component σ_x across the bar a) stresses at line $x = 0$, b) for several finite distances x.

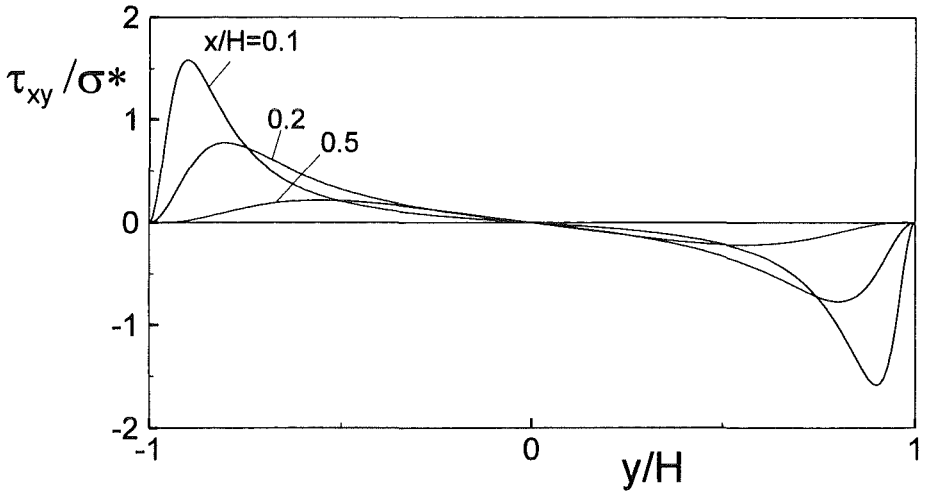

Fig. 7 Stress component τ_{xy} across the bar for several distances x.

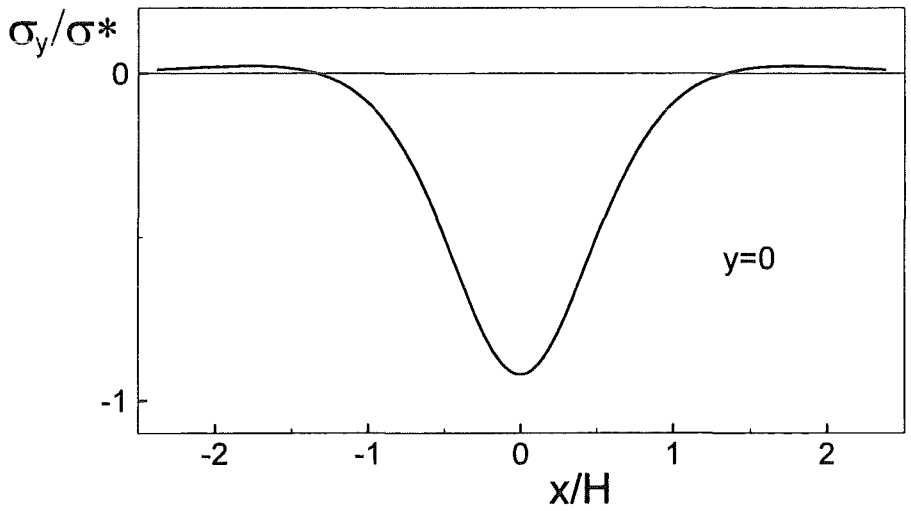

Fig. 8 Stress component σ_y along the centre line $y=0$.

The biaxial stress state at the centre ($x=y=0$) is characterised by

$$\sigma_x = 0.249\frac{P}{Ht}, \quad \sigma_y = -0.919\frac{P}{Ht}, \quad \tau_{xy} = 0 \tag{5}$$

with the ratio of the principal stresses

$$\sigma_2 / \sigma_1 = -3.7 \tag{6}$$

being quite similar to the Brazilian Disk test with

$$\sigma_2 / \sigma_1 = -3$$

The variation of the stress components σ_x and σ_y with the x-coordinate is plotted in Fig. 9a along the line $y=0$. The ratio of the principal stresses is given in Fig. 9b.

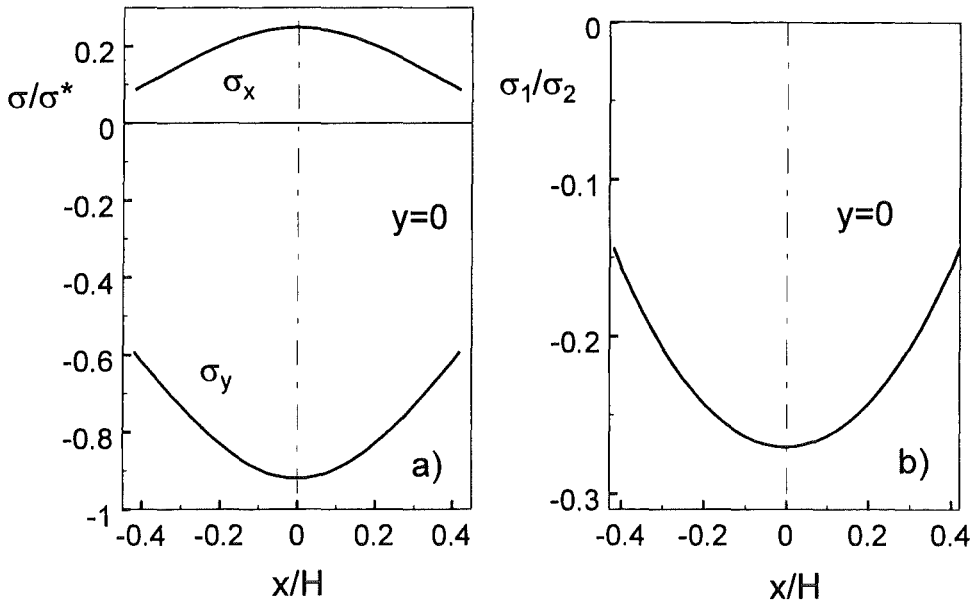

Fig. 9 Biaxiality of stresses in the centre of the plate.

2.2 Stresses caused by two pairs of concentrated forces

Superposition of the results given for one pair of concentrated forces enables to compute the loading problem illustrated in Fig. 10.

From eqs.(1)-(3) one obtains

$$\sigma_x = -\frac{4P}{\pi Ht}\int_0^\infty \frac{\sinh u - u\cosh u}{\sinh 2u + 2u}\cos\frac{ux}{H}\cos\frac{ud}{2H}\cosh\frac{uy}{H}\,du -$$

$$-\frac{4P}{\pi Ht}\int_0^\infty \frac{uy}{H}\frac{\sinh u}{\sinh 2u + 2u}\cos\frac{ux}{H}\cos\frac{ud}{2H}\sinh\frac{uy}{H}\,du \qquad (7)$$

$$\sigma_y = -\frac{4P}{\pi Ht}\int_0^\infty \frac{\sinh u + u\cosh u}{\sinh 2u + 2u}\cos\frac{ux}{H}\cos\frac{ud}{2H}\cosh\frac{uy}{H}\,du$$

$$+\frac{4P}{\pi Ht}\int_0^\infty \frac{uy}{H}\frac{\sinh u}{\sinh 2u + 2u}\cos\frac{ux}{H}\cos\frac{ud}{2H}\sinh\frac{uy}{H}\,du \qquad (8)$$

$$\tau_{xy} = \frac{4P}{\pi Ht}\int_0^\infty \frac{u\cosh u}{\sinh 2u + 2u}\sin\frac{ux}{H}\cos\frac{ud}{2H}\sinh\frac{uy}{H}\,du$$

$$-\frac{4P}{\pi Ht}\int_0^\infty \frac{uy}{H}\frac{\sinh u}{\sinh 2u+2u}\sin\frac{ux}{H}\cos\frac{ud}{2H}\cosh\frac{uy}{H}\,du \tag{9}$$

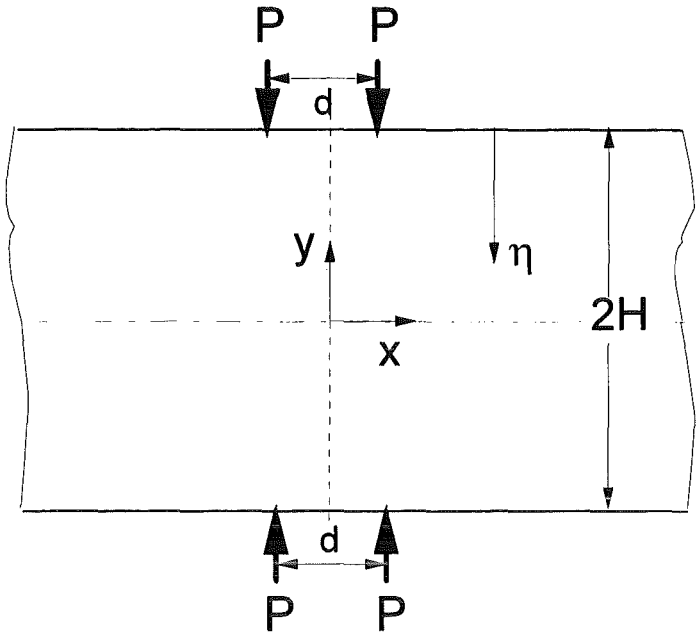

Fig. 10 Computation of stresses by the use of a symmetric 4-roller arrangement, $\eta = H\text{-}y$.

and for the symmetry line ($x = 0$)

$$\sigma_x = -\frac{4P}{\pi Ht}\int_0^\infty \frac{\sinh u - u\cosh u}{\sinh 2u+2u}\cos\frac{ud}{2H}\cosh\frac{uy}{H}\,du -$$

$$-\frac{4P}{\pi Ht}\int_0^\infty \frac{uy}{H}\frac{\sinh u}{\sinh 2u+2u}\cos\frac{ud}{2H}\sinh\frac{uy}{H}\,du \tag{10}$$

$$\sigma_y = -\frac{4P}{\pi Ht}\int_0^\infty \frac{\sinh u + u\cosh u}{\sinh 2u+2u}\cos\frac{ud}{2H}\cosh\frac{uy}{H}\,du$$

$$+\frac{4P}{\pi Ht}\int_0^\infty \frac{uy}{H}\frac{\sinh u}{\sinh 2u+2u}\cos\frac{ud}{2H}\sinh\frac{uy}{H}\,du \tag{11}$$

The resulting stresses σ_x and σ_y are plotted in Figs. 11 and 12. The shear stresses τ_{xy} disappear along the symmetry line.

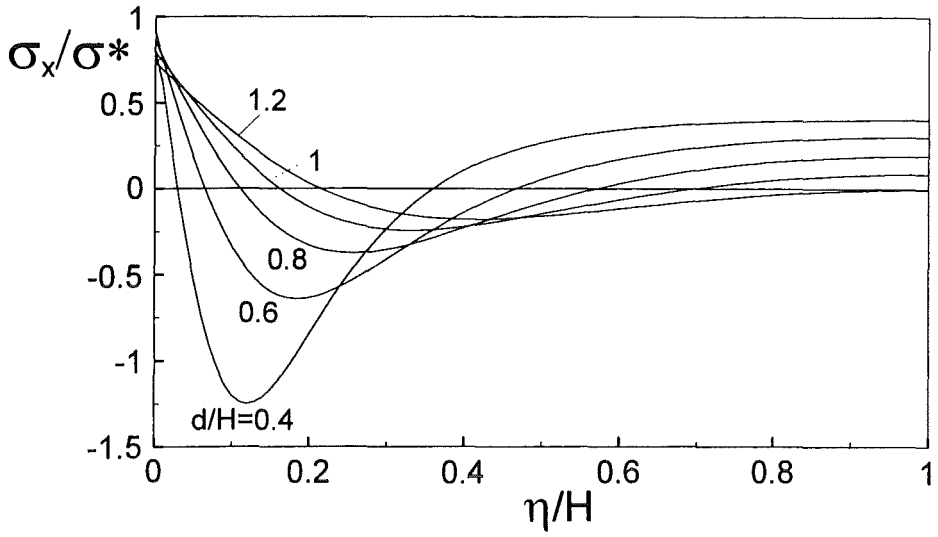

Fig. 11 Axial stresses σ_x along the symmetry line $x = 0$.

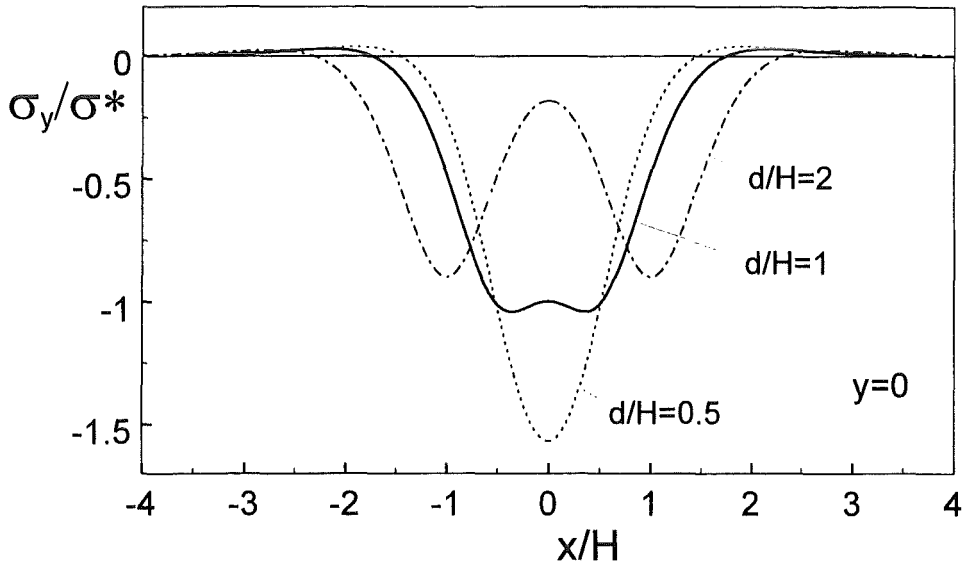

Fig. 12 Stress component σ_y along the centre line $y = 0$ for two pairs of concentrated forces.

2.3 Stresses caused by symmetrically distributed loads

Under real loading conditions by rollers, symmetric pressure distributions occur as shown for a single pair in Fig. 13. Therefore, we introduce the continuous pressure distribution $p(x')$ by

$$p(x') = p_0 f(x'), \qquad \text{with } f(x') = f(-x') \tag{12}$$

with a characteristic pressure value p_0, e.g. the pressure at $x' = 0$. In order to determine the related stress distributions in the material, we have to compute the stress distribution for a pair of symmetric pressure loads $\mathrm{d}P$

$$\mathrm{d}P(x') = p(x')\,\mathrm{d}x' + p(-x')\mathrm{d}x' \tag{13}$$

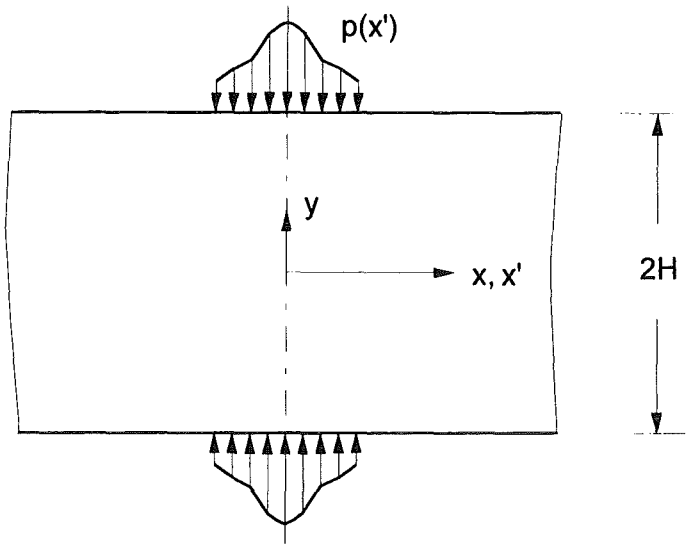

Fig. 13 Parallel strip loaded by opposite symmetric pressure distribution.

Integrating eqs.(7-9) results in

$$\sigma_x(x) = -\frac{4p_0}{\pi H}\int_0^{\infty}\left[\int_0^{\infty}\frac{\sinh u - u\cosh u}{\sinh 2u + 2u}\cos\frac{ux}{H}\cos\frac{ux'}{H}\cosh\frac{uy}{H}\,du\right]f(x')\,dx' -$$

$$-\frac{4p_0}{\pi H}\int_0^{\infty}\left[\int_0^{\infty}\frac{uy}{H}\frac{\sinh u}{\sinh 2u + 2u}\cos\frac{ux}{H}\cos\frac{ux'}{H}\sinh\frac{uy}{H}\,du\right]f(x')\,dx' \qquad (14)$$

$$\sigma_y = -\frac{4p_0}{\pi H}\int_0^{\infty}\left[\int_0^{\infty}\frac{\sinh u + u\cosh u}{\sinh 2u + 2u}\cos\frac{ux}{H}\cos\frac{ux'}{H}\cosh\frac{uy}{H}\,du\right]f(x')\,dx'$$

$$+\frac{4p_0}{\pi H}\int_0^{\infty}\left[\int_0^{\infty}\frac{uy}{H}\frac{\sinh u}{\sinh 2u + 2u}\cos\frac{ux}{H}\cos\frac{ux'}{H}\sinh\frac{uy}{H}\,du\right]f(x')\,dx' \qquad (15)$$

$$\tau_{xy} = \frac{4p_0}{\pi H}\int_0^{\infty}\left[\int_0^{\infty}\frac{u\cosh u}{\sinh 2u + 2u}\sin\frac{ux}{H}\cos\frac{ux'}{H}\sinh\frac{uy}{H}\,du\right]f(x')\,dx'$$

$$-\frac{4p_0}{\pi H}\int_0^{\infty}\left[\int_0^{\infty}\frac{uy}{H}\frac{\sinh u}{\sinh 2u + 2u}\sin\frac{ux}{2H}\cos\frac{ux'}{H}\cosh\frac{uy}{H}\,du\right]f(x')\,dx' \qquad (16)$$

where x' is the location where the stresses are evaluated.

A special case of a symmetrical load is the constant pressure p_0 over a region of width s, i.e.

$$p(x') = \begin{cases} p_0 & \text{for } |x'| \le s/2 \\ 0 & \text{for } |x'| > s/2 \end{cases} \tag{17}$$

i.e.

$$f(x') = \begin{cases} 1 & \text{for } |x'| \le s/2 \\ 0 & \text{for } |x'| > s/2 \end{cases} \tag{18}$$

as shown in Fig. 14. Let us here define the characteristic pressure p_0 by

$$p_0 = P / t\,s \tag{19}$$

In this case, integration over x' yields

$$\sigma_x = -\frac{2P}{\pi Ht}\int_0^\infty \frac{\sinh u - u\cosh u}{\sinh 2u + 2u}\cos\frac{ux}{H}\left(\frac{2H}{us}\sin\frac{us}{2H}\right)\cosh\frac{uy}{H}\,du -$$

$$-\frac{2P}{\pi Ht}\int_0^\infty \frac{uy}{H}\frac{\sinh u}{\sinh 2u + 2u}\cos\frac{ux}{H}\left(\frac{2H}{us}\sin\frac{us}{2H}\right)\sinh\frac{uy}{H}\,du \tag{20}$$

$$\sigma_y = -\frac{2P}{\pi Ht}\int_0^\infty \frac{\sinh u + u\cosh u}{\sinh 2u + 2u}\cos\frac{ux}{H}\left(\frac{2H}{us}\sin\frac{us}{2H}\right)\cosh\frac{uy}{H}\,du$$

$$+\frac{2P}{\pi Ht}\int_0^\infty \frac{uy}{H}\frac{\sinh u}{\sinh 2u + 2u}\cos\frac{ux}{H}\left(\frac{2H}{us}\sin\frac{us}{2H}\right)\sinh\frac{uy}{H}\,du \tag{21}$$

$$\tau_{xy} = \frac{2P}{\pi Ht}\int_0^\infty \frac{u\cosh u}{\sinh 2u + 2u}\left(\frac{2H}{us}\sin\frac{us}{2H}\right)\sin\frac{ux}{H}\sinh\frac{uy}{H}\,du$$

$$-\frac{2P}{\pi Ht}\int_0^\infty \frac{uy}{H}\frac{\sinh u}{\sinh 2u + 2u}\left(\frac{2H}{us}\sin\frac{us}{2H}\right)\sin\frac{ux}{H}\cos\frac{ud}{2H}\cosh\frac{uy}{H}\,du \tag{22}$$

Having in mind that

$$\left(\frac{2H}{us}\sin\frac{us}{2H}\right) \to 1 \quad \text{for} \quad \frac{us}{2H} \to 0 \tag{23}$$

we obtain relations (1)-(3) for the case of a concentrated pair of forces.

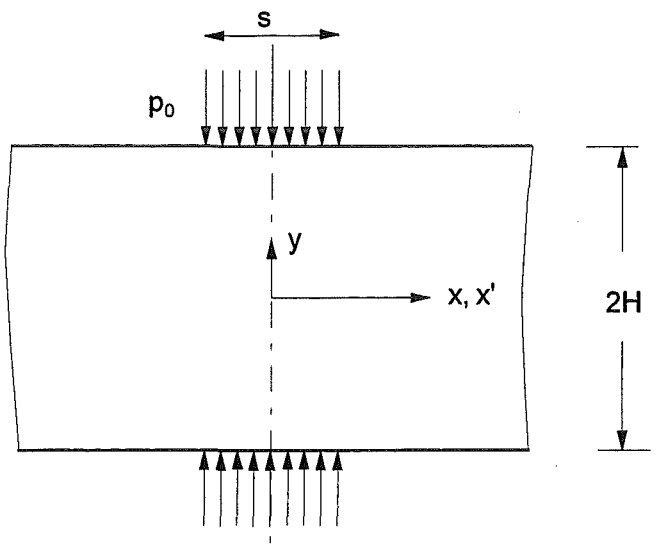

Fig. 14 Parallel strip loaded by a section of constant opposite symmetric pressure.

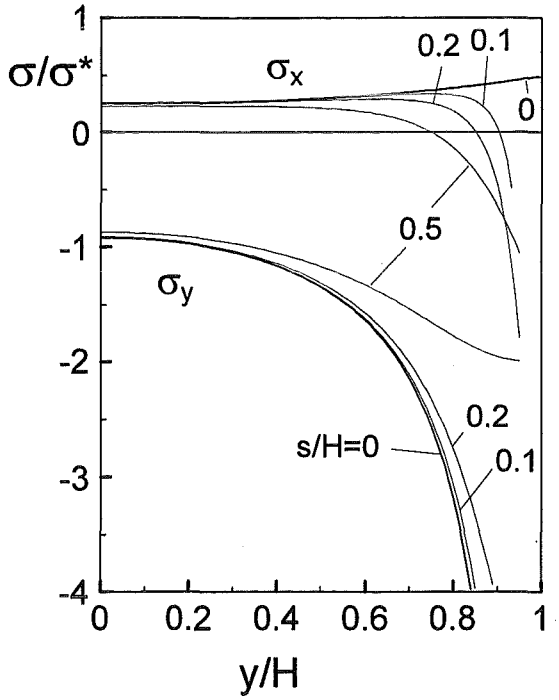

Fig. 15 Stresses along the symmetry axis ($x = 0$) for several widths of the pressurised zone.

The influence of a finite load contact area on the stress state is plotted in Fig. 15 along the symmetry axis, $x = 0$. For $s/H < 0.2$ and $y/H < 0.75$ the effect of a finite s is negligible. The curves of Fig. 15 are quite similar to those obtained for the Brazilian Disk test (see [4][5]).

3 Stress intensity factors for single-edge-cracked bars

The stress intensity factors for the cracked specimens can be computed from the stresses in the uncracked specimen using the fracture mechanics weight function. If σ_x are the stresses normal to the prospective crack line and τ are the shear stresses at the same location, the mode-I stress intensity factor K_I and the mode-II stress intensity factor K_{II} result from

$$K_I = \int_0^a \sigma_x(\eta)\, h_I(a,\eta)\, d\eta \tag{24}$$

$$K_{II} = \int_0^a \tau_{xy}(\eta)\, h_{II}(a,\eta)\, d\eta \tag{25}$$

($\eta = H\text{-}y$) with the mode-I and mode-II weight functions h_I and h_{II}. The weight functions for the edge-cracked bar can be taken from [7] (see eqs.(6.4.15) and (12.1.9)).

3.1 Computation of the stress intensity factors for 2-roller loading

First the stress intensity factors were computed for the case of two diametral forces P acting on an edge-cracked bar (see Fig. 16).

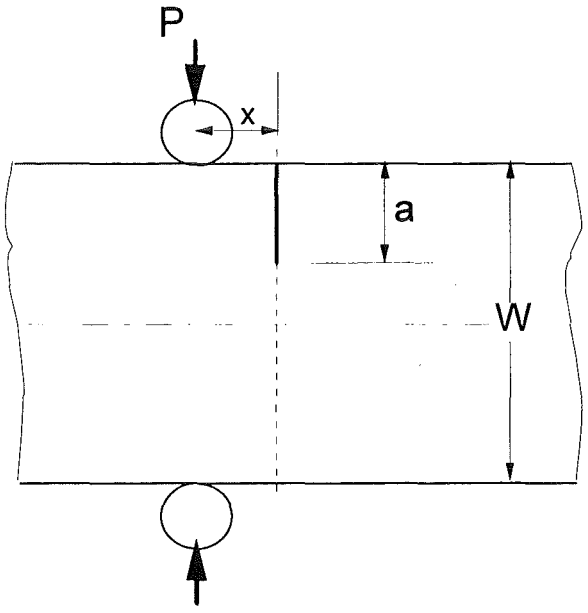

Fig. 16 Edge-cracked plate loaded by a single pair of opposite forces.

The geometric functions for the mode-I and mode-II stress intensity factors, here denoted as Y_I and Y_{II}, are defined by

$$K_I = \sigma * Y_I \sqrt{W} \tag{26a}$$

$$K_{II} = \sigma * Y_{II} \sqrt{W} \tag{26b}$$

Figures 17 and 18 show the results which are also compiled in Tables 1 and 2.

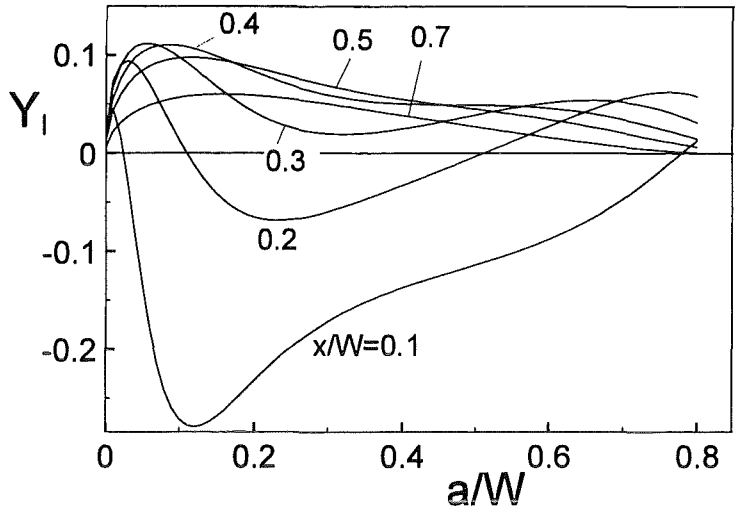

Fig. 17 Geometric function Y according to eq.(26a) for the 2-point loading.

a/W	*x/W*=0.1	0.2	0.3	0.4	0.5
0.1	-0.2718	0.0123	0.097	0.1096	0.0970
0.2	-0.2324	-0.0654	0.0415	0.0830	0.0872
0.3	-0.1717	-0.0596	0.020	0.0591	0.0687
0.4	-0.1375	-0.0329	0.025	0.0503	0.0549
0.5	-0.1142	-0.0033	0.039	0.0490	0.0449
0.6	-0.0879	0.0273	0.051	0.0457	0.0343
0.7	-0.047	0.055	0.052	0.0323	0.0205

Table 1 Mode-I stress intensity factors for 2-point loading, represented by the geometric function Y, eq.(26a).

a/W	*x/W*=0.05	0.1	0.15	0.2	0.25	0.3	0.4	0.5
0.1	1.433	0.660	0.296	0.134	0.0556	0.0147	-0.021	-0.031
0.2	1.340	0.560	0.634	0.392	0.226	0.117	0.0005	-0.044
0.3	1.185	0.942	0.712	0.506	0.337	0.205	0.0396	-0.037
0.4	1.083	0.876	0.686	0.510	0.358	0.232	0.0598	-0.028
0.5	1.029	0.814	0.625	0.459	0.318	0.205	0.0511	-0.027
0.6	1.012	0.754	0.542	0.371	0.238	0.140	0.0214	-0.032
0.7	1.020	0.673	0.418	0.242	0.128	0.0568	-0.012	-0.034

Table 2 Mode-II stress intensity factors for 2-point loading, represented by the geometric function Y_{II}, eq.(26b).

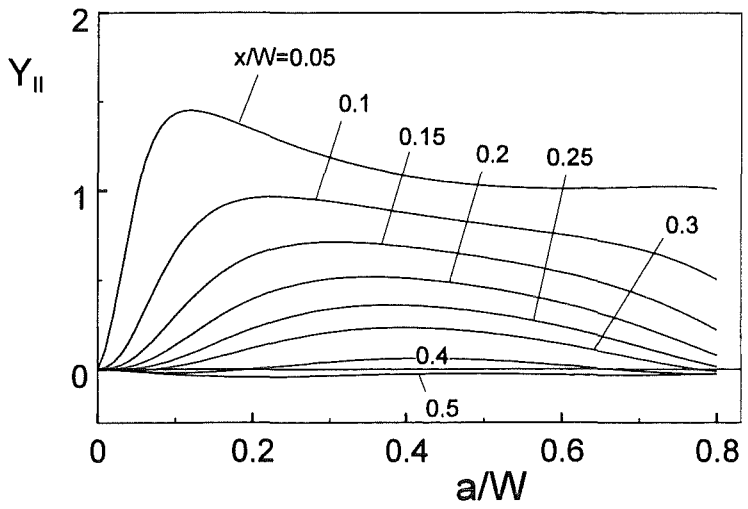

Fig. 18 Geometric function Y_{II} according to eq.(26b) for the 2-point loading.

3.2 Computation of the stress intensity factors for 4-roller loading

Let us first evaluate the stress intensity factor for the test device with four-point loading (Fig. 3). In this case, we have to identify the specimen width by $W = 2H$.

In the special case of the crack being located in the centre between the rollers ($x = 0$) it holds $\tau = 0$ through the whole bar and, consequently, $K_{II} = 0$. The mode-I stress intensity factor for this case is shown in Fig. 19 as a function of d/W and is entered in Table 3, expressed by the geometric function Y, defined by eq.(26a).

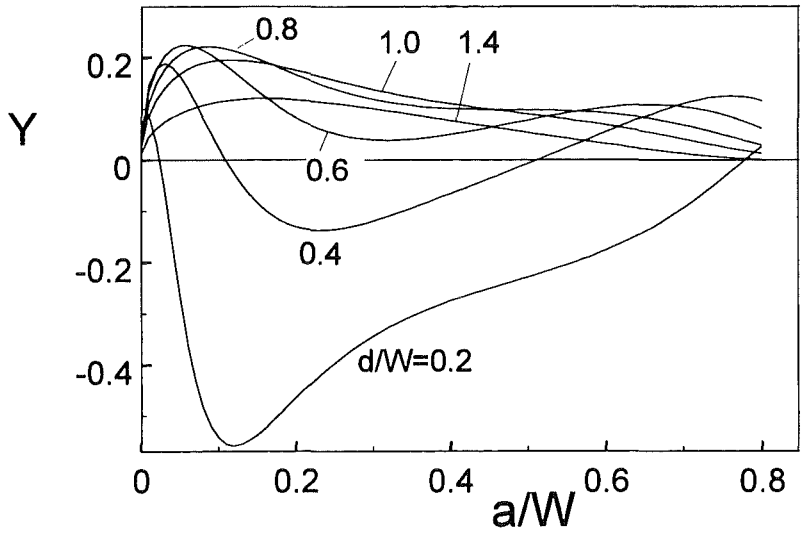

Fig. 19 Geometric function Y according to eq.(26) for the 4-point loading.

	d/W=0.2	0.4	0.6	0.8	1.0	1.2	1.4	1.6
a/W=0.05	-0.26	0.171	0.2234	0.2066	0.1686	0.1279	0.0916	0.0624
0.1	-0.537	0.034	0.1997	0.2196	0.1942	0.1538	0.1136	0.0792
0.15	-0.531	-0.337	0.1346	0.1971	0.1903	0.1578	0.1199	0.0854
0.2	-0.458	-0.077	0.0836	0.1660	0.1746	0.1510	0.1176	0.0853
0.25	-0.389	-0.1331	0.0526	0.1384	0.1556	0.1389	0.1103	0.0811
0.3		-0.117	0.0403	0.1186	0.1377	0.1250	0.1003	0.0743
0.35		-0.0915	0.0414	0.1068	0.1224	0.1110	0.0891	0.0660
0.4			0.0506	0.1011	0.1101	0.0977	0.0774	0.0569
0.45			0.0641	0.0991	0.0998	0.0850	0.0658	0.0419
0.5			0.0791	0.0984	0.0902	0.0727	0.0542	0.0382
0.55			0.0931	0.0968	0.0804	0.0606	0.0431	0.0291
0.6			0.1041	0.0924	0.0693	0.0483	0.0322	0.0207
0.65			0.1094	0.0838	0.0564	0.0359	0.0221	0.0131
0.7			0.1064	0.0703	0.0422	0.0239	0.0132	0.0068

Table 3 Stress intensity factors for 4-point loading, represented by the geometric function Y, eq.(26).

3.3 Crack extension under 4-roller loading

Knowledge of the stress intensity factor solution enables to predict crack growth under increasing load. For a material without an R-curve effect the crack propagation phases are illustrated in Fig. 20 for the special case of $d/W = 1$.

If the initial crack depth a_0 is smaller than the value a_m corresponding to the maximum stress intensity factor (Fig. 20a), crack extension is unstable up to a_1. Then, stable crack propagation takes place.

For an initial crack depth $a_0 \geq a_m$, stable crack growth occurs exclusively.

In case of a sufficiently steep R-curve, stable crack extension also appears for $a_0 < a_m$.

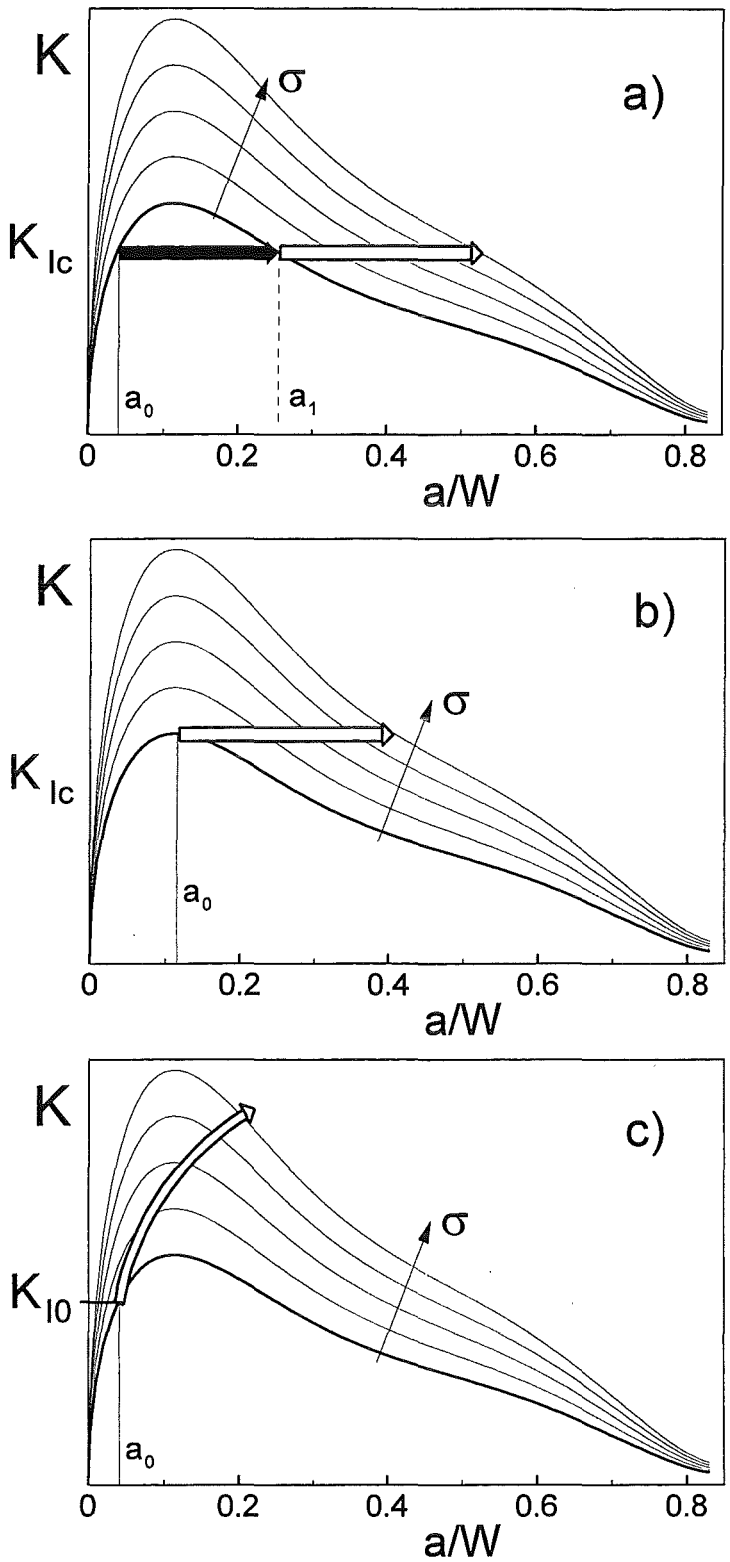

Fig. 20 Crack growth under increasing load; a) initial crack size $a_0 < a_m$, b) $a_0 = a_m$, c) $a_0 < a_m$, increasing R-curve.

3.4 Stress intensity factors for 2-roller loading and flat supporting

In order to perform simple analytical calculations, the stresses for the original problem, shown in Fig. 2, can be approximated by the stresses in the uncracked body under 4-point loading. Therefore, we consider the supporting area of the *uncracked specimen* of width W as the symmetry line of a specimen with thickness $2W$ loaded by 4 rollers, as illustrated in Fig. 21. Friction effects are ignored completely in this approximation.

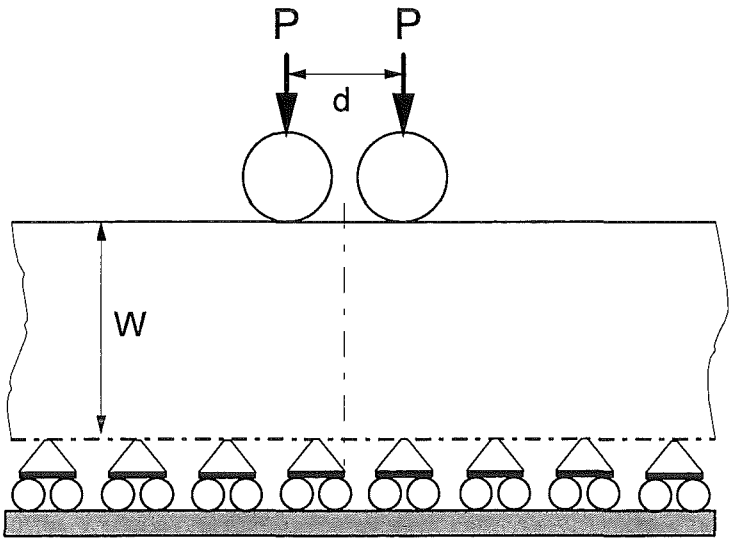

Fig. 21 Approximation of the bar loaded by two point forces and bedded on a rigid material by half of the bar loaded by four opposite point forces.

In this approximation the same stress solution holds as represented by eqs.(7)-(9), with $W = H$ and

$$\sigma^* = \frac{P}{Wt} \tag{27}$$

The solution is not exact as can be seen from Fig. 12. The stress component σ_y is not compressive for all locations on the symmetry line. In the case of $d/H = 1$, low tensile stresses occur for $x/H > 1.7$. In the specimen of half thickness, the supporting conditions cannot cause tensile stresses. The prescription of full contact over the whole supporting length therefore violates the real boundary conditions for the half specimen bedded on a semi-infinite body.

The approximative stress intensity factors are plotted in Fig. 22 and additionally entered in Table 4.

For $d/W \leq 1.25$ the stress intensity factor first increases and then decreases. For $d/W < 0.9$ negative stress intensity factors occur. In the case of $d/W > 1.25$, monotonically increasing curves are obtained.

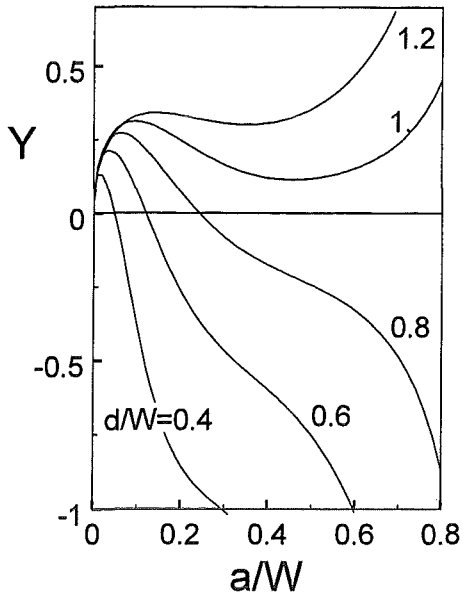

Fig. 22 Geometric function Y according to eq.(26a) for different roller distances.

	d/W=0.4	0.6	0.8	1.0	1.2
a/W=0.05	0.0074	0.2131	0.2728	0.285	0.285
0.1	-0.3760	0.0746	0.2473	0.3140	0.3324
0.15	-0.6735	-0.1052	0.1652	0.2903	0.3418
0.2	-0.8426	-0.2609	0.0722	0.2479	0.3329
0.25		-0.3773	-0.0112	0.2035	0.3186
0.3		-0.4620	-0.0784	0.1658	0.3069
0.35		-0.5287	-0.1302	0.1384	0.3025
0.4			-0.1707	0.1221	0.3081
0.45			-0.2051	0.1164	0.3259
0.5			-0.2385	0.1206	0.3577
0.55			-0.2757	0.1341	0.4064
0.6			-0.3222	0.1575	0.4768

Table 4 Geometric function Y according to eq.(26a) for 2-point loading.

3.5 Crack extension under 2-roller loading

In the case of a material without an R-curve behaviour, the crack extension for an initial crack of depth a_0 under increasing load can be described as:

- In the case of the curves for d/W = 0.4-0.8, unstable crack extension occurs at a certain stress (see Fig. 23). The crack size after the spontaneous crack extension is a_1. With increasing loads applied the crack then propagates in a stable manner. Due to the fact that

positive stress intensity factors are limited (e.g. to $a \approx 0.25$ for $d/W = 0.8$), the maximum possible crack length is $a \approx 0.25$.

- For $0.9 < d/W < 1.25$ we first find unstable crack propagation (see Fig. 24) from a_0 to a_1. Then, further crack growth is stable up to a critical crack length a_c which is reached at the critical stress σ_c. Further crack extension is unstable.

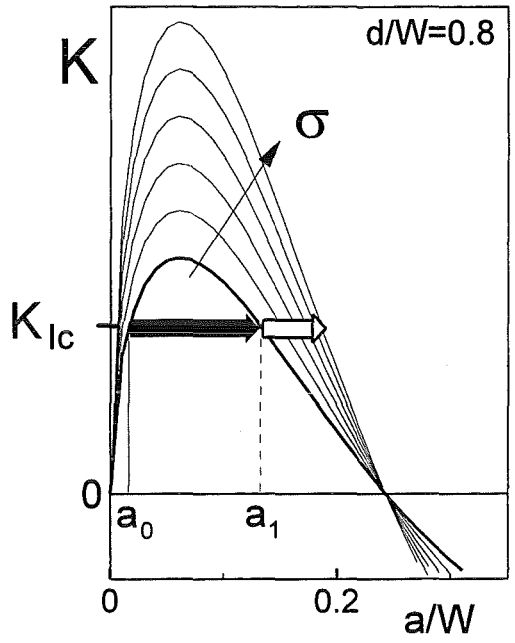

Fig. 23 Unstable and stable crack extension during increasing loading for $d/W = 0.8$; solid arrow: Unstable crack propagation, open arrow: Stable crack growth.

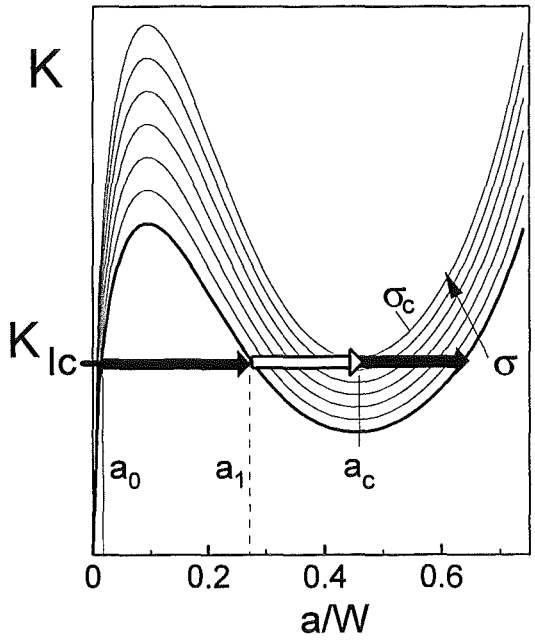

Fig. 24 Phases of unstable and stable crack extension during increasing loading for $d/W = 1$; solid arrows: Unstable crack propagation, open arrow: Stable crack growth.

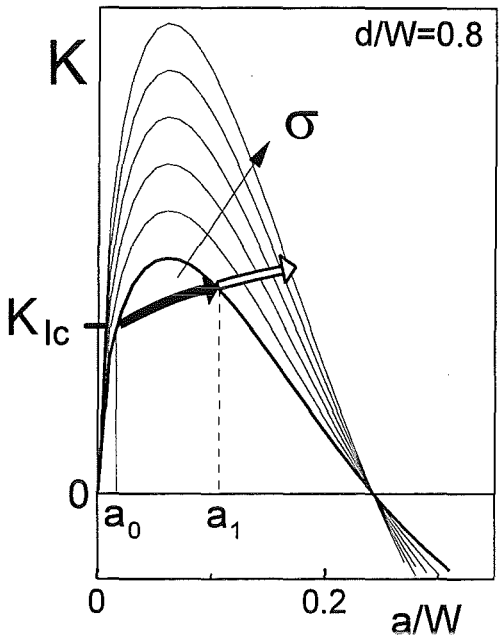

Fig. 25 Unstable and stable crack extension during increasing loading for a material with a rising R-curve ($d/W = 0.8$); solid arrow: Unstable crack propagation, open arrow: Stable crack growth.

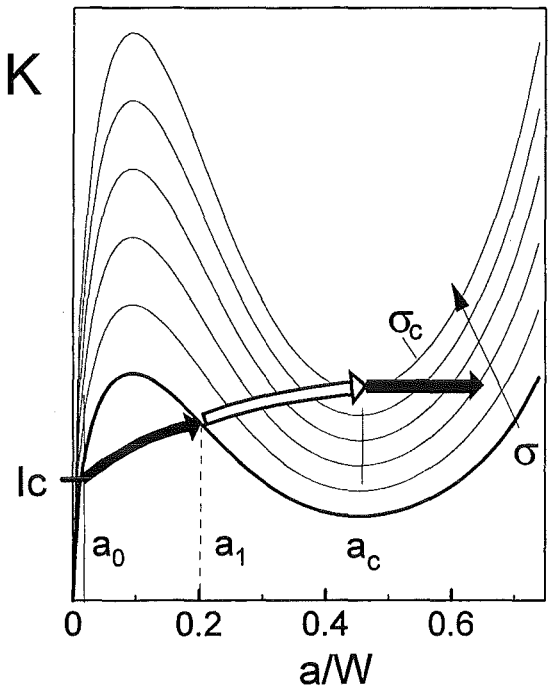

Fig. 26 Phases of unstable and stable crack extension during increasing loading for a material with a rising R-curve ($d/W = 1$); solid arrows: Unstable crack propagation, open arrow: Stable crack growth.

In the case of a material with an increasing crack resistance, the same principal crack propagation characteristics are obtained. Figures 25 and 26 show the crack extension phases similar to Figs. 23 and 24. The only differences are the reduced unstable crack extension phases.

3.6 Loading-point compliance for 4-point loading

To evaluate the R-curves from crack extension tests under 4-point roller loading, it is necessary to know the actual crack depth a. The determination of a can be done either by optical observation using a travelling microscope or by use of the compliance. From the relation between the energy release rate G_I, the stress intensity factor K_I, and the compliance C

$$G_I = \frac{P_{appl}^2}{2t}\frac{dC}{da} = \frac{K_I^2}{E'}, \qquad P_{appl} = 2P \tag{28}$$

with $E' = E/(1-\nu^2)$, one can determine the compliance from the stress intensity factor solution represented in Fig. 19 and Table 3 by simple integration

$$C' = 2\int_0^{\alpha} Y^2 \, d\alpha' \quad , \quad \alpha = a/W \tag{29}$$

with the normalised compliance C', given by

$$C' = E' t C \tag{30}$$

This contribution of compliance is only caused by the existence of a crack. The total compliance is the sum of this part and of the compliance of the uncracked specimen. The compliance C' is plotted in Fig. 27. Numerical results are also compiled in Table 5. From Fig. 27 we expect that the compliance evaluation is sufficiently sensitive up to about a/W=0.4.

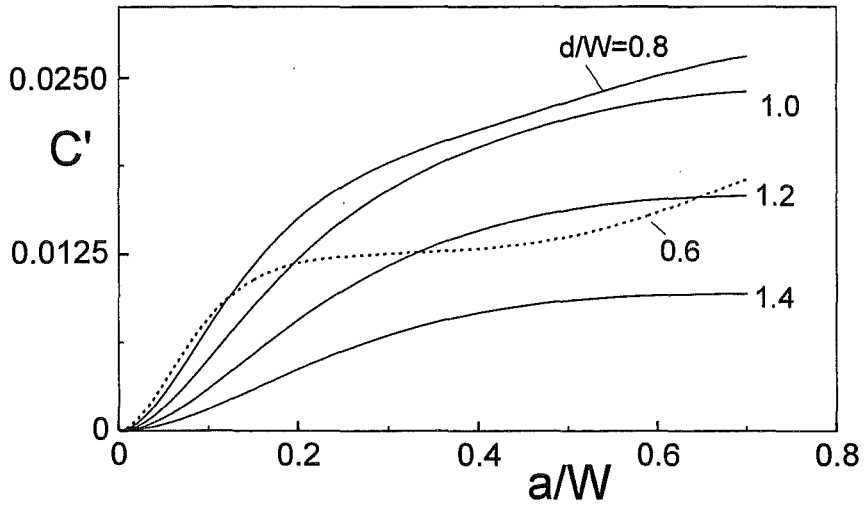

Fig. 27 Contribution of loading-point compliance for the 4-roller device, caused by the crack.

	d/W=0.8	1.0	1.2	1.4
a/W=0.05	0.0026	0.0016	0.0009	0.0005
0.1	0.0073	0.0051	0.0030	0.0016
0.15	0.0117	0.0088	0.0054	0.0029
0.2	0.0150	0.0123	0.0078	0.0044
0.25	0.0173	0.0149	0.0099	0.0057
0.3	0.0190	0.0170	0.0117	0.0068
0.35	0.0202	0.0187	0.0131	0.0077
0.4	0.0213	0.0201	0.0142	0.0084
0.45	0.0223	0.0212	0.0150	0.0089
0.5	0.0233	0.0221	0.0156	0.0092
0.55	0.0242	0.0228	0.0161	0.0095
0.6	0.0251	0.0234	0.0164	0.0096
0.65	0.0259	0.0238	0.0166	0.0097
0.7	0.0265	0.0240	0.0167	0.0097

Table 5 Normalised compliance C' for 4-point loading.

4 Double-edge-cracked bars

In this section the mode-I stress intensity factors are computed for a double-edge-cracked bar under 4-roller loading. The specimen and load application are illustrated in Fig. 28. The procedure of the stress intensity factors is very similar to the single-edge-cracked specimens considered in the preceding sections. The only difference is the use of the special weight function for double-edge cracks in eq.(24), available from handbooks on stress intensity factors and weight functions [7-9].

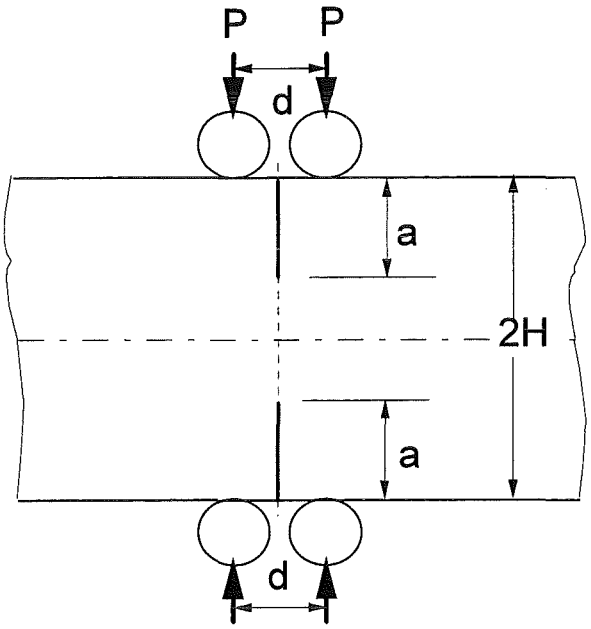

Fig. 28 Double-edge-cracked bar loaded by two pairs of opposite forces.

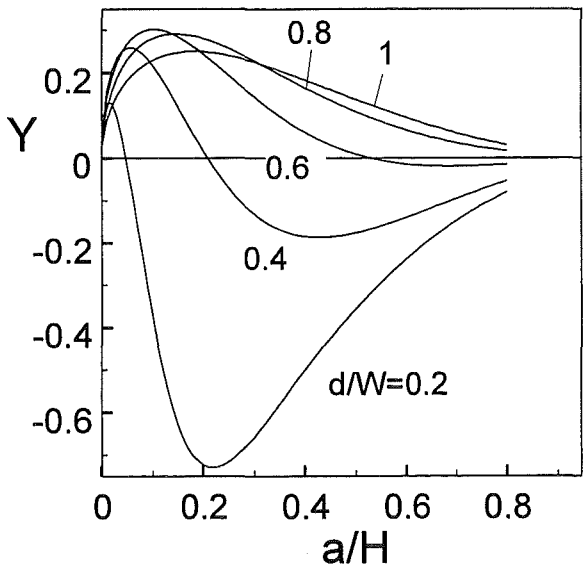

Fig. 29 Geometric function Y according to eq.(31) for different roller distances.

The stress intensity factor solution is plotted in Fig. 29 and compiled for a number of crack depths in Table 6. Since $H = W/2$ is the characteristic width dimension for normalising the crack length a (i.e. a is limited by $a < H$) in case of double-edge-cracked bars, let us define here the stress intensity factor by

$$K = \sigma * Y\sqrt{H} \tag{31}$$

a/W	d/W=0.2	0.4	0.6	0.8	1.0
0.05	-0.016	0.258	0.267	0.230	0.182
0.1	-0.374	0.218	0.302	0.280	0.229
0.15	-0.627	0.121	0.285	0.291	0.248
0.2		0.017	0.244	0.281	0.250
0.3		-0.132	0.144	0.229	0.226
0.4		-0.185	0.061	0.165	0.184
0.5		-0.177	0.009	0.109	0.138
0.6		-0.140	-0.015	0.065	0.095
0.7		-0.095	-0.020	0.035	0.059
0.8		-0.054	-0.015	0.016	0.031

Table 6 Mode-I stress intensity factors for double-edge-cracked bars under 4-point loading, represented by the geometric function Y, eq.(31).

5 Experimental setups

5.1 Loading device for fracture toughness tests

An experimental setup for a fracture mechanics test is shown in Fig. 30. A pre-notched bar is loaded by four rollers in order to create a sharp crack. The load P_{appl} is applied to the upper rollers by a half-sphere. In order to keep the location of the rollers fixed in all tests, they are drawn outside using soft rubber strings (not plotted in Fig. 30). As rollers cylindrical pins (hardened steel) may be used. A simple procedure allows to estimate the R-curve without any further equipment.

Pre-notched bending bars are monotonously loaded. From a load vs. time record, the moment of first crack extension can be detected as a pop-in of the load. After a further increase of load, the test is suspended. After unloading, the actual crack length can be measured at the side surfaces using an optical microscope. Application of a penetration dye also allows to measure the crack depth on the fracture surface of a broken specimen. From the applied load P at the moment of unloading, the crack depth a, the geometric function Y (obtained by interpolation of Table 3), and the stress intensity factor K_{IR} present at the moment of unloading can be computed using eq.(26a). A series of tests suspended at different loads then provides the R-curve $K_{IR}=f(\Delta a)$. For the evaluation of eqs.(26a) and (4) we have to use $P=P_{appl}/2$.

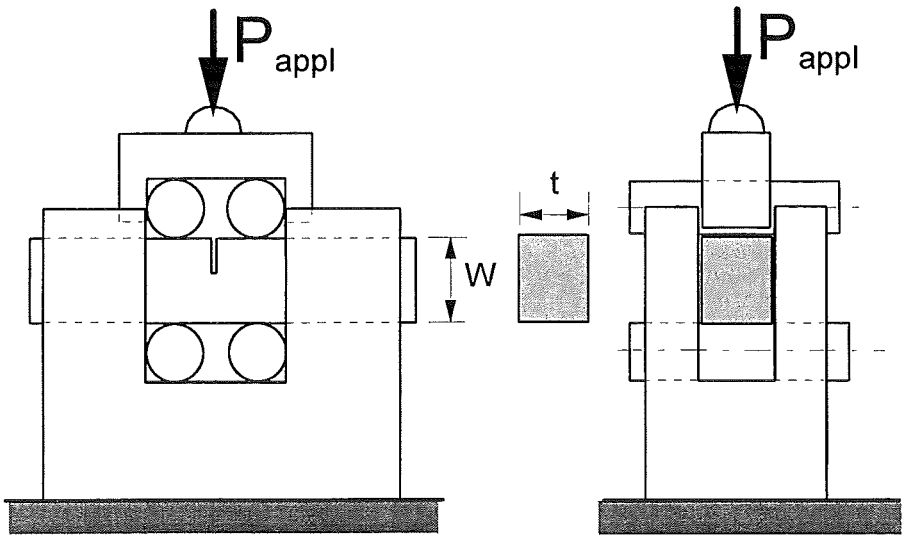

Fig. 30 Device for a 4-roller crack extension test.

5.2 Devices for strength tests under contact loading

Test devices for contact strength tests (similar to Fig. 30) are illustrated in Fig. 31. Two rollers opposite to the rectangular specimen are loaded by a force P. The rollers (made of hardened steel) are about 0.1 mm smaller than the guide groove in the supporting structure in order to

avoid any clamping during load application (cylinders become oval under load). The 4-roller device (Fig. 30) proposed for fracture mechanics tests can also be applied for contact strength tests.

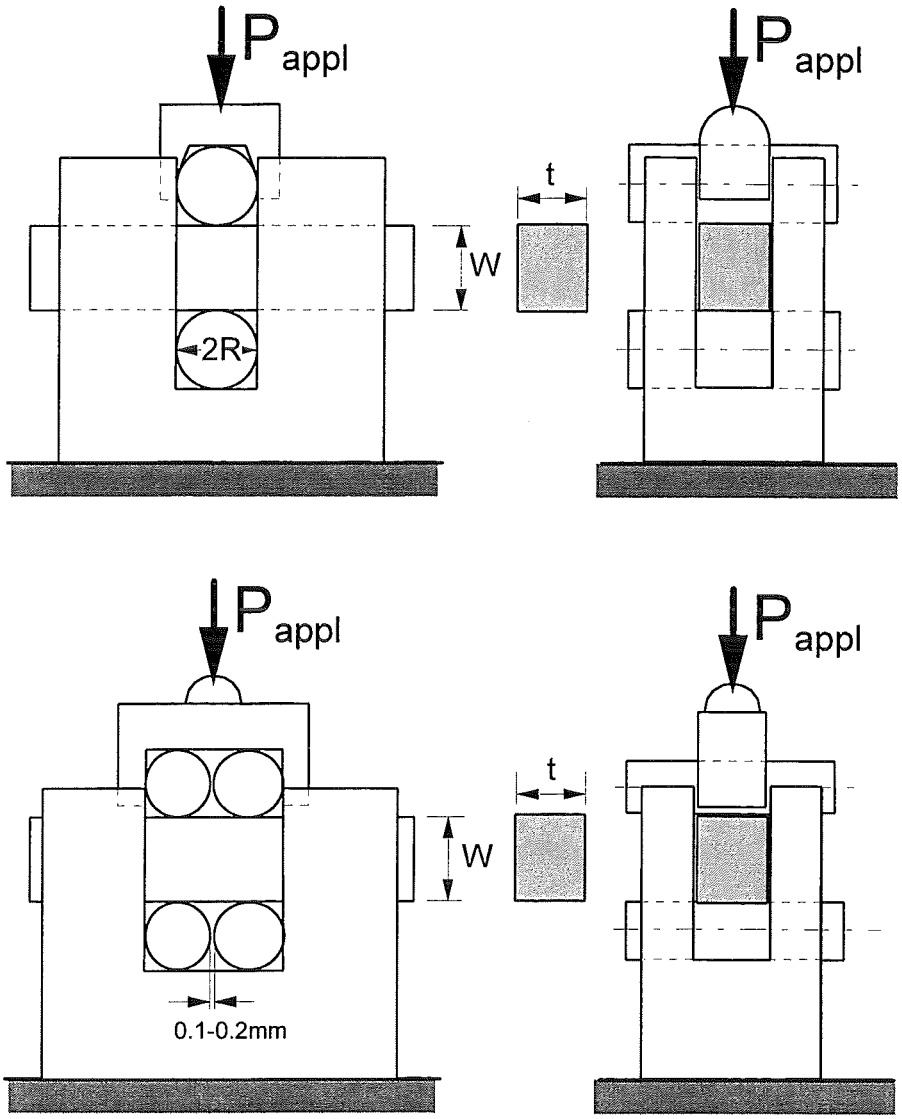

Fig. 31 Test devices for contact strength tests (2-roller and 4-roller arrangements).

In the case of a 2-roller testing device, the maximum tensile stress is reached at $x = 0$ and $y = \pm H$, i.e. directly below the rollers. At these locations, it holds

$$\sigma_{max} = 0.992 \frac{P_{appl}}{Wt} \tag{32}$$

For the 4-point loading device with $d/W = 1$ we obtain the maximum tensile stresses below the rollers with

$$\sigma_{max} = 0.518 \frac{P_{appl}}{Wt} \tag{33}$$

In Fig. 32 the σ_x-components for the two test devices are plotted for the surface $y = H$ and for a depth slightly below the surface ($y/H = 0.995$). The stress component σ_x at the surface of the 4-point loaded bar is very similar to the stress distribution along the surface of a bar in a 4-point bending test.

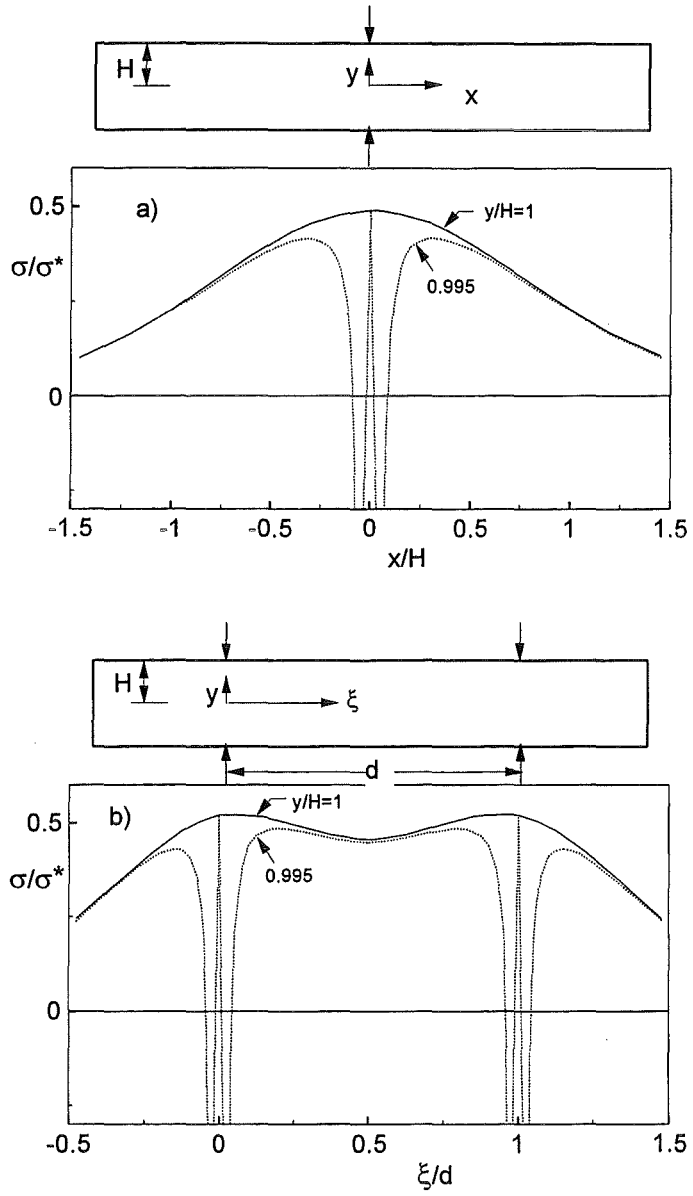

Fig. 32 Surface and near-surface stresses (stress component σ_x) for a) 2-roller test, b) 4-roller test.

Failure under contact loading may start from crack-like defects in the volume of the test specimen due to the very high compressive stresses near the contact lines between the rollers and the specimen and from surface flaws introduced during machining. In order to distinguish between the failure events in the central part of the specimen and failure near the surface, a simple electrical circuit may be modified as proposed in [10]. As shown by Fig. 33, two thin

conductive strips are applied on the side surface of a specimen. Each of the brittle strips is considered a closed logical switch (denoted as S_1 and S_2) which is opened if fracture occurs.

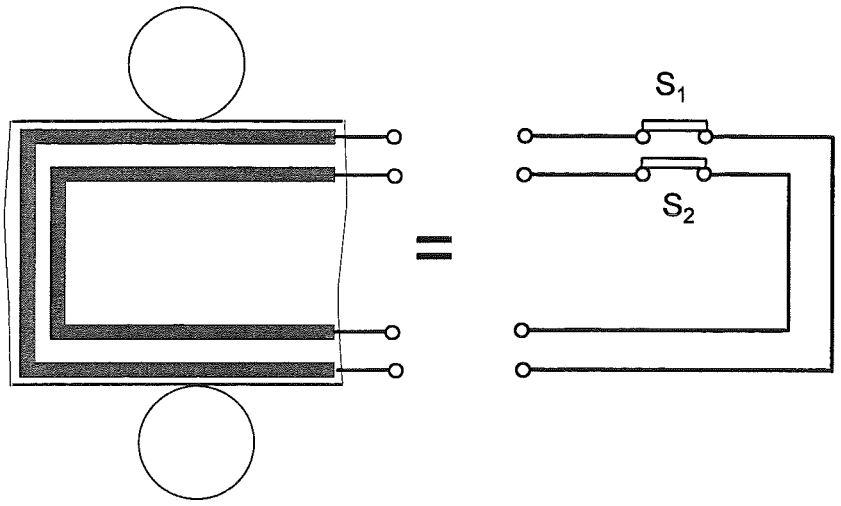

Fig. 33 Brittle conductive strips acting as logical switches S_1, S_2.

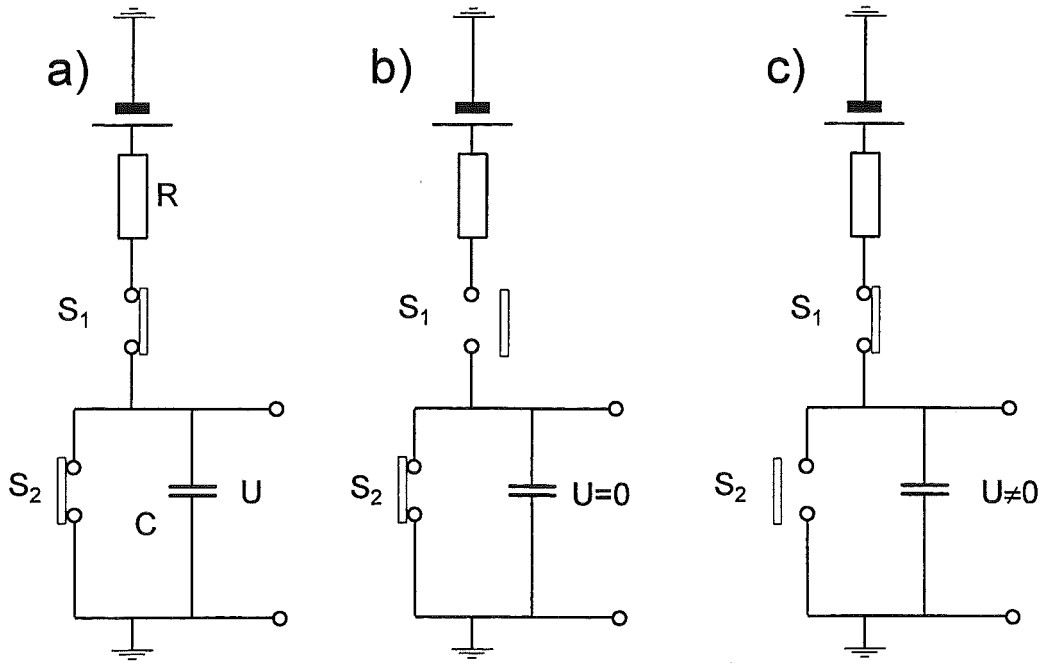

Fig. 34 Sequence of switch opening and output signals; a) both switches closed, b) switch S_1 opens before switch S_2 (crack starts from the outer region), c) switch S_2 opens before switch S_1 (crack starts from the inner region).

The two switches are fit in an electrical circuit as shown in Fig. 34a. A battery of voltage U_0 causes a current through the resistor R and the switches S_1 and S_2. In this case, a capacitor C is short-circuited by S_2 and its voltage U is zero. Under increasing mechanical load, failure of

the specimen occurs. First let us consider the case of failure starting near the roller contact zone. From Fig. 33 we see that the outer strip must fail first, e.g. first the switch S_1 must open (see Fig. 34b). As the consequence, the voltage is disconnected and no effect on the capacitor can be expected. If failure starts from the centre region of the specimen, the switch S_2 opens first and the capacitor is loaded by the current $i = U/R$ until the switch S_1 opens. In this case, a voltage occurs at the capacitor, which may be recorded with an X-Y-recorder. Due to the high input resistance of the recorder, the electrical signal is present for a time long enough to record it. Now, it is very easy to decide whether failure started in the central region (an output signal is recorded) or whether an irregular result was obtained (no output signal detectable).

If the actual failure location has to be determined, it is necessary to apply an increased number of conductive layers. On one of the side surfaces a number of horizontal strips is placed and on the opposite side vertical strips are attached. A logical network as used in [11] enables to determine the fracture origin.

The expected failure diagram is shown by Fig. 35. Figure 36 shows the failure diagram for the Brazilian Disk test. Both tests describe similar stress states.

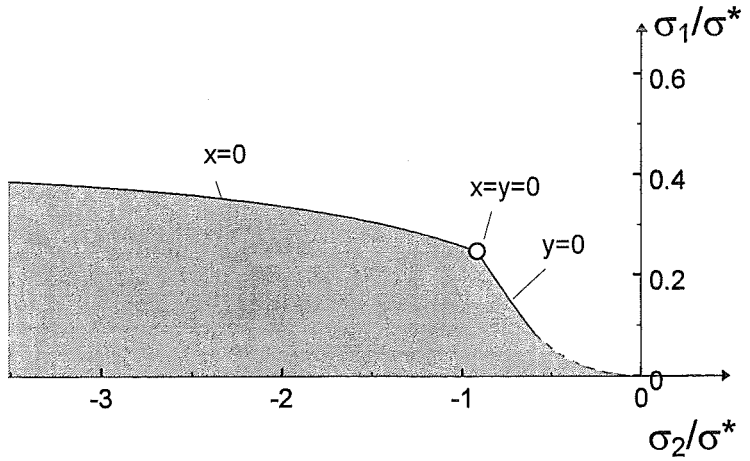

Fig. 35 Multiaxial stress state in a bar loaded by a pair of opposite forces (2-roller arrangement in Fig. 31).

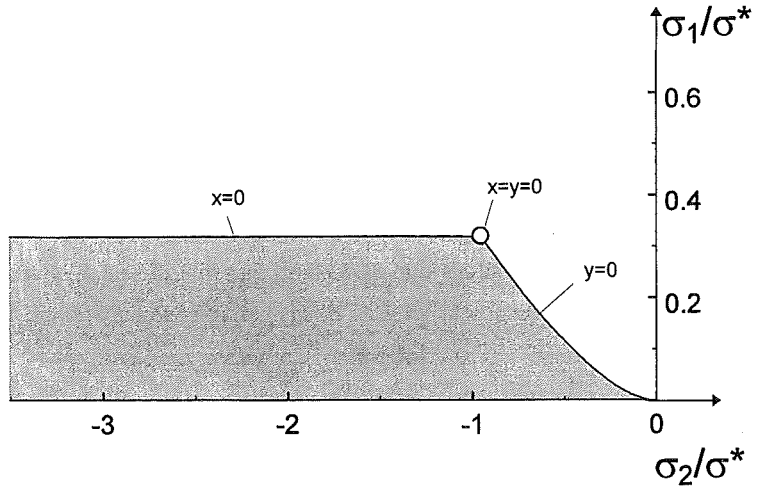

Fig. 36 Multiaxial stress state in a Brazilian disk (with $\sigma^* = P/(Rt)$).

A direct comparison of the failure diagrams is given in Fig. 37 where only the curves for $x = 0$ and $y = 0$ are plotted.

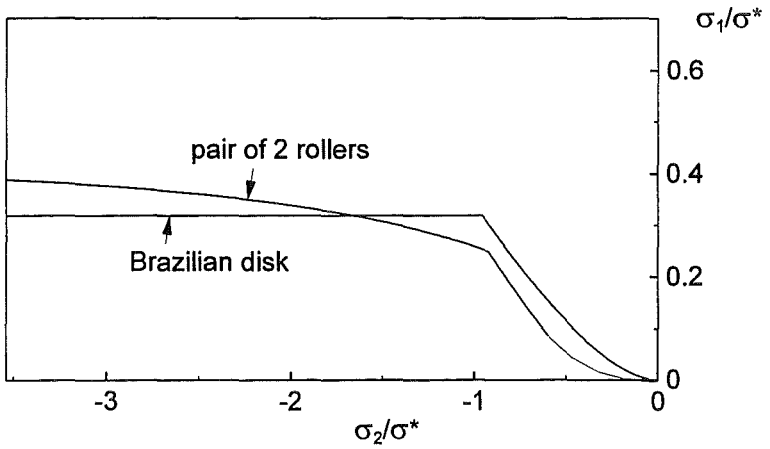

Fig. 37 Comparison of stress states.

6 Experimental results

6.1 Strength measurements

As examples of application, contact strength tests were performed on two types of commercial aluminum oxides and a PZT ceramic using the roller arrangements given in Fig. 31.

Material (I) is an alumina containing about 4 wt% glass phase (V38, CeramTec, Plochingen), material (II) is a coarse-grained alumina (Al23, Friatec, Friedrichsfeld).
Material (III) is a soft PZT ceramic (PIC 151, PI Ceramic).

As "strength", the maximum σ_x-stresses according to eqs.(32) and (33) were used in the roller tests. Failure can be noticed by a clear acoustic shock, accompanied by a pop-in in the load vs. time plot. For reasons of comparison, 4-point bending tests were carried out in addition.

6.1.1 Strength of Al_2O_3

The measured strength data are represented in Fig. 38. Based on the relation for the failure probability F

$$F = 1 - \exp[-(\sigma_c / \sigma_0)^m] \tag{34}$$

the Weibull parameters m and σ_0 were determined with the "Maximum Likelihood Procedure" according to [12] and are given in Table 7.

The 90% confidence intervals (represented by the data in brackets) were computed as suggested in [13]. The correction of the Weibull parameters m was performed according to [12], resulting in the unbiased Weibull exponent m_{corr} listed in the last column of Table 7. A typical fracture is shown in Fig. 38.

Material	Test	σ_0 (MPa)	m	m_{corr}
(I)	4-roller test	183.4 [175.; 193.]	9.8 [6.5; 12.6]	9.0
	2-roller test	238.2 [220.8; 257.3]	5.7 [4.0; 7.2]	5.3
	bending test	315.6 [307.0; 324.6]	19.7 [12.1; 26.0]	17.6
(II)	4-roller test	219.8 [210.6; 229.4]	10.0 [6.9; 12.6]	9.2
	2-roller test	329.2 [311.8; 348.2]	8.2 [5.5; 10.5]	7.6
	bending test	274.8 [262.6; 288.0]	12.6 [7.5; 16.7]	11.1

Table 7 Weibull parameters for the strength of the aluminas.

The strengths under 4-roller loading are about 60% for material (I) and about 80% of the bending strengths for material (II). In the case of the 2-roller loading we find for material (I) ≅75% and 120% for material (II). The Weibull exponents m are reduced in the roller tests.

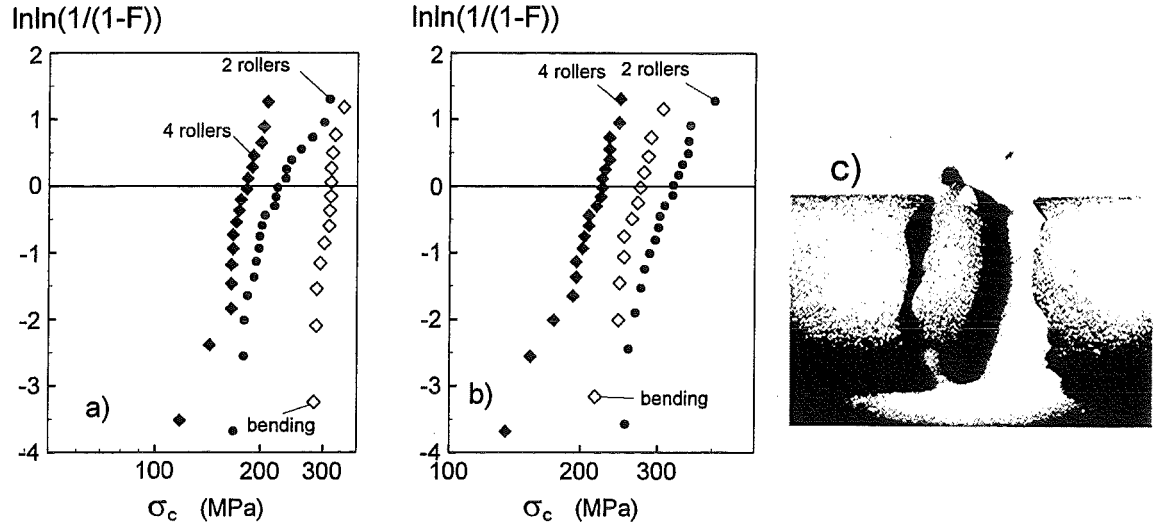

Fig. 38 Contact strengths obtained with the 4-roller device of Fig. 30 (solid squares) and the 2-roller device (circles), compared with 4-point bending strength (open squares); a) Al_2O_3 with 4% glass phase (material I), b) coarse-grained Al_2O_3 (material II), c) typical fracture under 2-roller loading.

6.1.2 Strength of PZT

Bars made of PZT ceramic (material III) were tested in flat and upright position. In the case of the poled material, tests were carried out with short-circuited electrodes (see Figs. 39a and c). In another test series, the free side was additionally covered by silver layers (Figs. 39b and d).

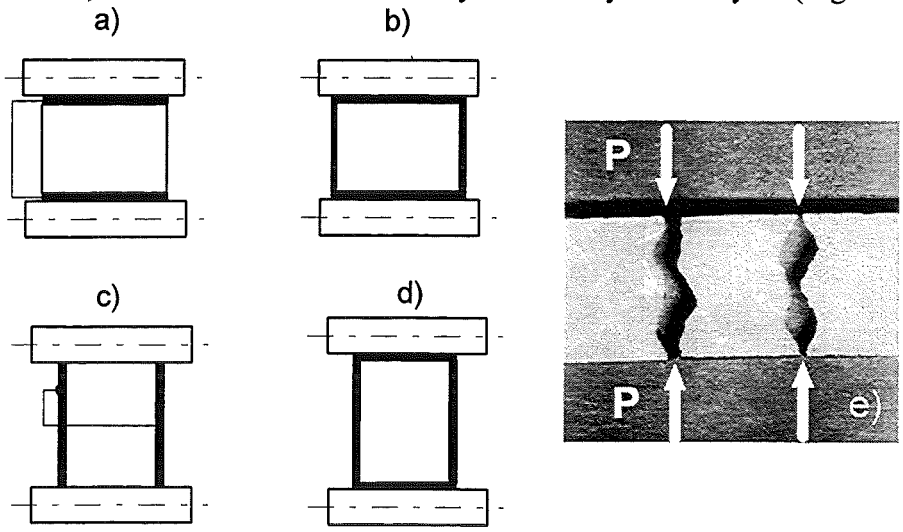

Fig. 39 4-roller strength tests for poled PZT; a), b) flat specimen position, c), d) upright specimen position, a) and c) electrodes short-circuited, b) and d) free sides additionally covered by silver layers; e) typical fracture of PZT under 4-roller loading

In Fig. 40 the strength results obtained with the 4-roller test device are shown. For the unpoled material, the results, for the flat and upright specimen position are in agreement. In the case of the poled material, the results for the specimens with short-circuited electrodes are nearly identical in both specimen positions. Significant strength reductions are obtained for the completely shielded specimens. Whereas for the upright position a strength reduction of about

20% is found, a strong reduction of about 50% is obvious in the flat position. These special effects will be discussed elsewhere. A typical fracture is shown in Fig. 39e.

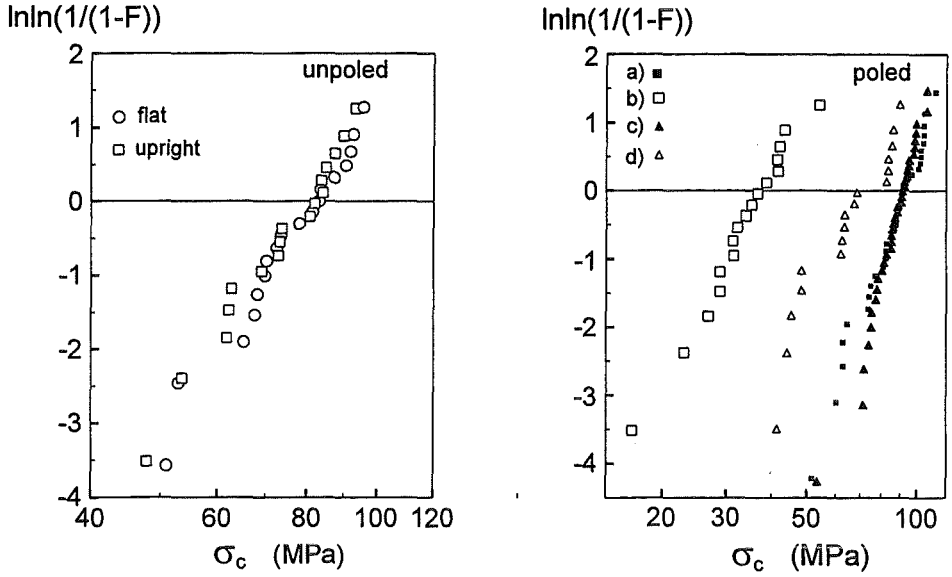

Fig. 40 Contact strength results obtained with 4-roller device and specimens according to Fig. 39.

In Fig. 41 the contact strength data are compared with bending strength data presented in [14]. In case of the unpoled material, the strengths for the flat and upright position are identical. The same holds for the poled material with short-circuited electrodes. Therefore, we collected the results for the upright and flat specimen positions within always one strength series.

Material	Test	Position	σ_0 (MPa)	m	m_{corr}
unpoled	bending test		75.3 [73.5; 77.2]	15.3 [11.1; 18.9]	9.7
	2-roller test	flat	108.0 [101.2; 114.2]	7.7 [5.3; 9.7]	7.1
	4-roller test	flat	81.6 [76.8; 87.0]	7.2 [4.9; 9.2]	6.6
		upright	79.4 [74.4; 85.0]	7.2 [4.8; 9.2]	6.6
⊥-poled	bending test		66.6 [64.5; 68.5]	13.4 [9.3; 16.9]	11.4
	2-roller test	a)	98.0 [90.4; 106.4]	5.2 [3.6; 6.6]	4.8
	4-roller test	a)	94.8 [91.4; 98.4]	8.4 [6.4; 10.1]	8.0
		b)	37.6 [33.8; 42.0]	4.4 [2.9; 5.7]	4.0
		c)	89.0 [85.8; 92.2]	8.4 [6.5.7; 10.8]	7.8
		d)	72.2 [65.6; 79.8]	4.8 [3.2; 6.2]	4.4

Table 8 Weibull parameters for the strength of PIC 151.

For the unpoled material the contact strength values were found to be identical with the bending strength and for the poled material the contact strength was 140% of the bending strength. In this context it has to be mentioned that the non-linear and non-symmetric stress

vs. strain behaviour may influence the contact strength results and the bending results differently (see also [15]).

Results of strength tests carried out with the 2-roller device are also represented in Table 8 and in Fig. 41. These results were obtained with flat specimen position and in case of the poled material with short-circuited electrodes.

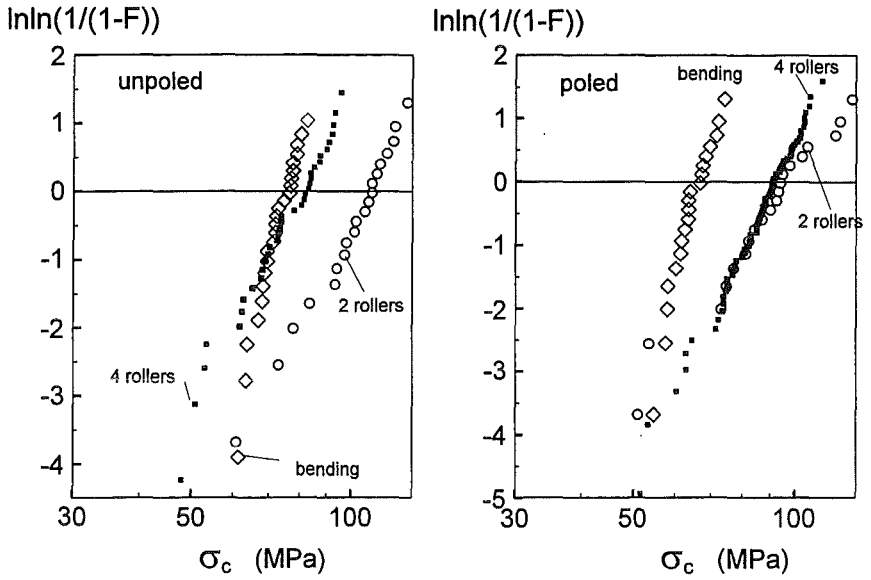

Fig. 41 Comparison of contact strength tests (squares: 4-roller tests, circles: 2-roller tests) with bending tests (diamond squares) for unpoled and poled PZT.

6.2 Fracture toughness

In order to demonstrate the applicability of the 4-roller test device, Fig. 30, measurements of the crack growth resistance were carried out with PIC 151. V-notches within a range of depths of a = 0.5-0.55mm were introduced into unpoled and ⊥-poled specimens of 3×4×45 mm^3(polarisation perpendicular to the specimen length axis) by use of the razor blade procedure [1]. Then, the specimens were loaded in the 4-roller testing device with $d/W = 1$ up to different forces. After unloading, the cracks generated were marked with a penetration dye and could be measured easily under the optical microscope following fracturing providing the final crack depth a. From the total maximum load $P_{appl} = 2P$ and the related crack length a, the stress intensity factor K_R was computed according to eq.(26) with the geometric function Y taken from Table 3 by use of a cubic spline interpolation. The results are plotted in Fig. 42.

From this representation we can conclude that the steepness of the R-curves is much less than obtained in controlled 3-point bending tests with single edge-notched bars [16] and in tests with compact tension (CT) specimens [17]. These differences will be discussed in a separate paper.

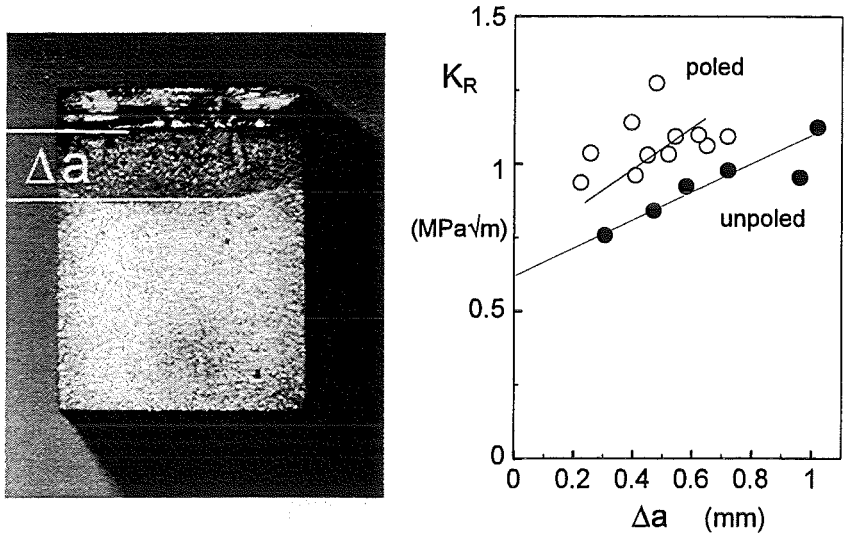

Fig. 42 Crack resistance K_R (R-curve) for unpoled and ⊥-poled PZT PIC 151 as a function of crack extension.

References

[1] Nishida, T., Pezzotti, G., Mangialardi, T., Paolini, A.E., Fracture mechanics evaluation of ceramics by stable crack propagation in bend bar specimens, Fracture Mechanics of Ceramics **11**(1996), 107-114.

[2] Warren, R., Johannesson, B., Creation of stable cracks in hard metals using 'bridge' indentation, Powder Metallurgy **27** (1984), 25-29.

[3] Nose, T., Fujii, T., Evaluation of fracture toughness for ceramic materials by a single-edge-precracked-beam method, J. Am. Ceram. Soc. **71** (1988), 328-333.

[4] Wright, P.J.F., Comments on an indirect tensile test on concrete cylinders, Magazine of Concrete Research, 7 (1955), 87–96.

[5] Munz, D., Fett, T., CERAMICS, Failure, Material Selection, Design, Springer-Verlag, März 1999.

[6] Filon, L.N.G., On an approximate solution for the bending of a beam of rectangular cross-section under any system of load, with special reference to points of concentrated or discontinuous loading, Phil. Trans., A, **201**(1903), 63-155.

[7] Fett, T., Munz, D., Stress intensity factors and weight functions, Computational Mechanics Publications, 1997, Southampton, UK.

[8] Tada, H., Paris, P.C., Irwin, G.R., The Stress Analysis of Cracks Handbook, Del Research Corporation, 1986.

[9] Wu, X.R., Carlsson, A.J., Weight functions and stress intensity factor solutions, Pergamon Press, Oxford 1991.

[10] Racké, H.H., Fett, T., Eine neue Schlagbiegeprüfung für Kunststoffe mit elektronischer Messung der Dehnung bei Bruchbeginn sowie der Bruchausbreitungsgeschwindigkeit, Kunststoffe **64**(1974), 481-487.

[11] Brückner-Foit, A., Fett, T., Munz, D., Schirmer, K.S., Discrimination of multiaxiality criteria with the Brazilian Disc test, J. Europ. Ceram. Soc. **17**(1997), 689-696.

[12] Thoman, D.R., Bain, L.J., Antle, C.E., Inferences on the parameters of the Weibull distribution, Technometrics **11**(1969), 445.

[13] European Standard ENV 843-5, Advanced monolithic ceramics - mechanical tests at room temperature - statistical analysis

[14] Fett, T., Munz, D., Thun, G., Tensile and bending strength of piezoelectric ceramics, to appear in J. Mater. Sci. Letters.

[15] Fett, T., Munz, D., Thun, G., Differences in bending and tensile strength for soft PZT, Proceedings 9th Cimtec, Part E, pp. 299-306, 1998.

[16] Fett, T., Munz, D., Thun, G., Fracture toughness and R-curve behaviour of PZT, FZKA-Report 6058, Forschungszentrum Karlsruhe 1998.

[17] Lucato, S.L., Lupascu, D.C., Rödel, J., Effect of poling direction on R-curve behavior in PZT, to be published in J. Am. Ceram. Soc.

[18] Timoshenko, S.P., Goodier, J.N., Theory of Elasticity, McGraw-Hill Kogagusha, Ltd., Tokyo.

[19] Fett, T., T-stresses in rectangular plates and circular disks, Engng. Fract. Mech. **60**(1998), 631-652.

Appendix

A1. Influence of specimen length on the stress state

A bar (or plate) of finite length $2L$ is illustrated in Fig A1. A pair of opposite concentrated forces P is applied at the distance d from the centre line.

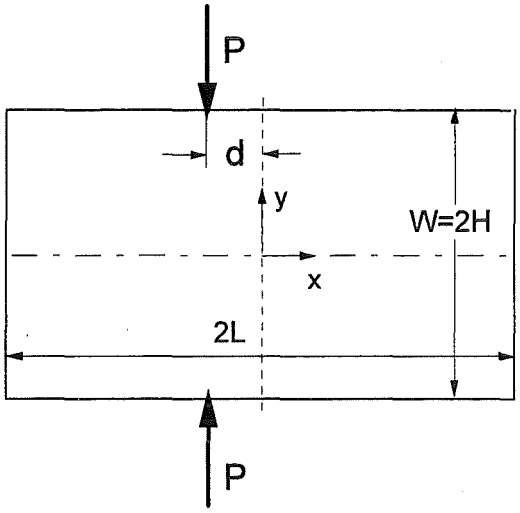

Fig. A1 Plate of finite length loaded by a pair of opposite forces.

The stresses in a rectangular plate are analytically known for any stress distribution $q_u(x)$ at the upper and $q_l(x)$ at the lower surface. It results (see e.g. Timoshenko and Goodier [18]) $\alpha = m\pi/L$

$$\sigma_x = \sum_{m=0}^{\infty}(A_m + B_m)\frac{(\alpha H\cosh\alpha H - \sinh\alpha H)\cosh\alpha y - \alpha y\sinh\alpha y\sinh\alpha H}{\sinh 2\alpha H + 2\alpha H}\sin\alpha x +$$

$$+(A_m - B_m)\frac{(\alpha H\sinh\alpha H - \cosh\alpha H)\sinh\alpha y - \alpha y\cosh\alpha y\cosh\alpha H}{\sinh 2\alpha H - 2\alpha H}\sin\alpha x +$$

$$+\sum_{m=0}^{\infty}(A'_m + B'_m)\frac{(\alpha H\cosh\alpha H - \sinh\alpha H)\cosh\alpha y - \alpha y\sinh\alpha y\sinh\alpha H}{\sinh 2\alpha H + 2\alpha H}\cos\alpha x +$$

$$+(A'_m - B'_m)\frac{(\alpha H\sinh\alpha H - \cosh\alpha H)\sinh\alpha y - \alpha y\cosh\alpha y\cosh\alpha H}{\sinh 2\alpha H - 2\alpha H}\cos\alpha x \qquad \text{(A1)}$$

$$\sigma_y = -\sum_{m=0}^{\infty}(A_m + B_m)\frac{(\alpha H\cosh\alpha H + \sinh\alpha H)\cosh\alpha y - \alpha y\sinh\alpha y\sinh\alpha H}{\sinh 2\alpha H + 2\alpha H}\sin\alpha x +$$

$$+(A_m - B_m)\frac{(\alpha H\sinh\alpha H + \cosh\alpha H)\sinh\alpha y - \alpha y\cosh\alpha y\cosh\alpha H}{\sinh 2\alpha H - 2\alpha H}\sin\alpha x -$$

$$-\sum_{m=0}^{\infty}(A'_m + B'_m)\frac{(\alpha H\cosh\alpha H + \sinh\alpha H)\cosh\alpha y - \alpha y\sinh\alpha y\sinh\alpha H}{\sinh 2\alpha H + 2\alpha H}\cos\alpha x +$$

$$+(A'_m - B'_m)\frac{(\alpha H\sinh\alpha H + \cosh\alpha H)\sinh\alpha y - \alpha y\cosh\alpha y\cosh\alpha H}{\sinh 2\alpha H - 2\alpha H}\cos\alpha x \qquad \text{(A2)}$$

$$\tau_{xy} = \sum_{m=0}^{\infty}(A_m + B_m)\frac{\alpha H\cosh\alpha H\sinh\alpha y - \alpha y\cosh\alpha y\sinh\alpha H}{\sinh 2\alpha H + 2\alpha H}\cos\alpha x +$$

$$(A_m - B_m)\frac{\alpha H\sinh\alpha H\cosh\alpha y - \alpha y\sinh\alpha y\cosh\alpha H}{\sinh 2\alpha H - 2\alpha H}\cos\alpha x -$$

$$-\sum_{m=0}^{\infty}(A'_m + B'_m)\frac{\alpha H\cosh\alpha H\sinh\alpha y - \alpha y\cosh\alpha y\sinh\alpha H}{\sinh 2\alpha H + 2\alpha H}\sin\alpha x +$$

$$-(A'_m - B'_m)\frac{\alpha H\sinh\alpha H\cosh\alpha y - \alpha y\sinh\alpha y\cosh\alpha H}{\sinh 2\alpha H - 2\alpha H}\sin\alpha x \qquad \text{(A3)}$$

The Fourier coefficients are given by

$$A'_m = \frac{1}{L}\int_{-L}^{L} q_u(x)\cos\frac{m\pi x}{L}dx \qquad \text{(A4a)}$$

$$B'_m = \frac{1}{L}\int_{-L}^{L} q_l(x)\cos\frac{m\pi x}{L}dx \qquad \text{(A4b)}$$

$$A_m = \frac{1}{L}\int_{-L}^{L} q_u(x)\sin\frac{m\pi x}{L}dx \qquad \text{(A4c)}$$

$$B_m = \frac{1}{L}\int_{-L}^{L} q_l(x)\sin\frac{m\pi x}{L}dx \qquad \text{(A4d)}$$

If we now introduce an opposite pair of point forces by traction distributions using the Dirac δ-function

$$q_l(x) = q_u(x) = P\delta(x - L) \qquad \text{(A5)}$$

the coefficients simply result as

$$A'_m = B'_m = \frac{P}{L}\cos\frac{m\pi d}{L}, \quad A_m = B_m = \frac{P}{L}\sin\frac{m\pi d}{L} \qquad \text{(A6)}$$

The most interesting σ_x stress component reads

$$\sigma_x = \sum_{m=1}^{\infty} \frac{2P}{Lt} \sin\frac{m\pi d}{L} \frac{(\alpha H \cosh\alpha H - \sinh\alpha H)\cosh\alpha y - \alpha y \sinh\alpha y \sinh\alpha H}{\sinh 2\alpha H + 2\alpha H} \sin\alpha x +$$

$$+\sum_{m=1}^{\infty} \frac{2P}{Lt} \cos\frac{m\pi d}{L} \frac{(\alpha H \cosh\alpha H - \sinh\alpha H)\cosh\alpha y - \alpha y \sinh\alpha y \sinh\alpha H}{\sinh 2\alpha H + 2\alpha H} \cos\alpha x \quad \text{(A7)}$$

In order to illustrate the influence of a finite specimen length $2L$, the σ_x stress component was computed for $d=0$ and $x=0$. The results are shown in Fig. A2. In Fig. A2b the tensile stress at the centre of the bar ($y=0$) is shown. From this representation we may conclude that the stress state in the centre is unaffected for a relative specimen length of $L/W > 1.5$. From this point of view, strength tests as well as fracture toughness tests can be performed with specimens of half the normal bending bar length.

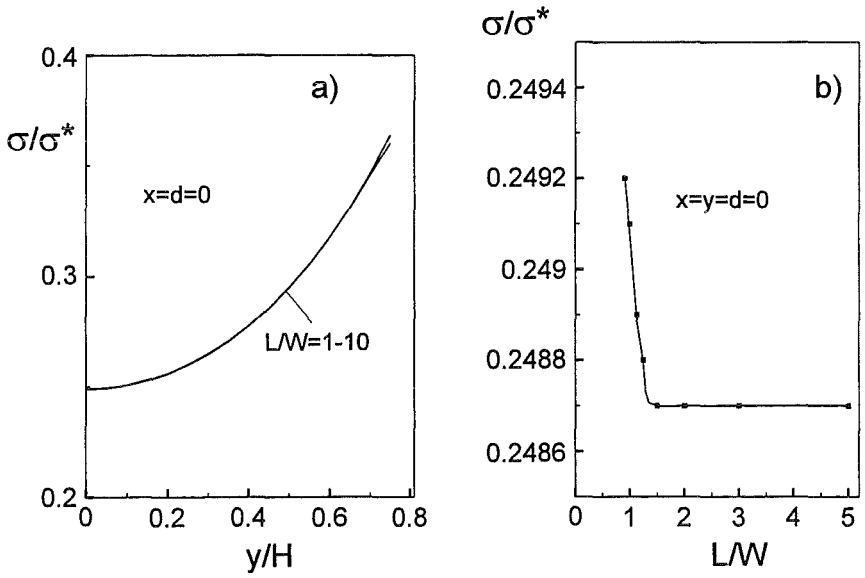

Fig. A2 Influence of the specimen length on the σ_x stress: a) stress distribution at $x=0$, b) stress value at the specimen centre ($x=y=0$).

A2 The T-stress term

Taking into consideration the singular stress term and the first regular term, the near-tip stress field of a cracked body can be described by

$$\sigma_{ij} = \frac{K_I}{\sqrt{2\pi r}} f_{ij}(\varphi) + \sigma_{ij,0} \quad \text{(A8)}$$

$$\sigma_{ij,0} = \begin{pmatrix} \sigma_{xx,0} & \sigma_{xy,0} \\ \sigma_{yx,0} & \sigma_{yy,0} \end{pmatrix} = \begin{pmatrix} T & 0 \\ 0 & 0 \end{pmatrix} \quad \text{(A9)}$$

where f_{ij} are the well-known angular functions for the singular stress contribution. The constant stress term is called the "T-stress". T-stress solutions for concentrated loads were computed in [19]. For a crack between two pairs of loads (see Fig. 3) the normalised T-stresses T/σ^* are given in Table 8.

$\alpha=a/W$	$d/W=0.2$	0.4	1	1.4	2	3
0.2	-2.48	-0.584	0.1044	0.0713	0.026	0.002
0.3	-2.44	-1.169	0.1064	0.1386	0.063	0.006
0.4	-2.28	-1.390	0.0660	0.1758	0.090	0.008
0.5	-2.22	-1.448	0.0438	0.1859	0.100	0.010
0.6	-2.28	-1.401	0.0650	0.1768	0.090	0.008
0.7	-2.47	-1.188	0.1180	0.1466	0.066	0.006

Table 8 T-stress T/σ^* for the edge-cracked strip under two pairs of opposite concentrated forces according to Fig. 3 [19].

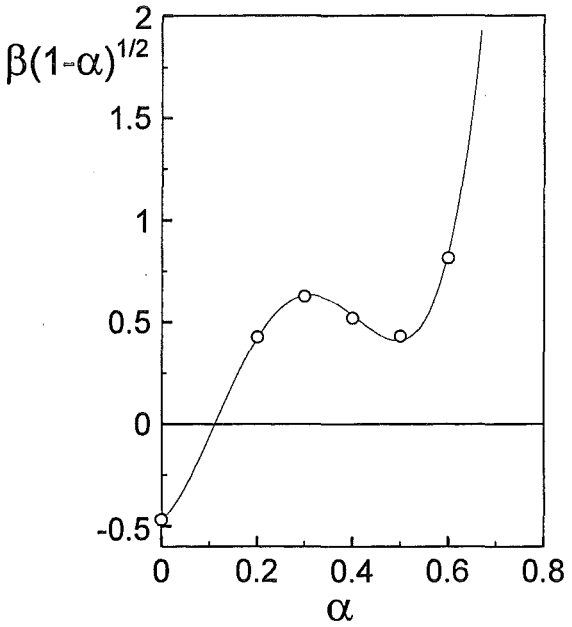

Fig. A3 Biaxiality ratio β for $d/W=1$.

In Fig. A3 the T-stress is represented by the biaxiality ratio β which is given by the ratio of T-stress and stress intensity factor according to

$$\beta = \frac{T\sqrt{\pi a}}{K_I} \tag{A10}$$

The curve given in Fig. A3 can be described by

$$\beta = \frac{-0.469 + 1.8589\alpha + 34.527\alpha^2 - 133.477\alpha^3 + 127.994\alpha^4}{\sqrt{1-\alpha}} \tag{A11}$$

A3 Maximum principal stress and maximum shear stress

From the stress components, eqs.(1)-(3), the principal stresses were computed. The first (maximum) principal stress σ_1 is shown in Fig. A4. The maximum shear stress τ_{max} is represented in Fig. A5.

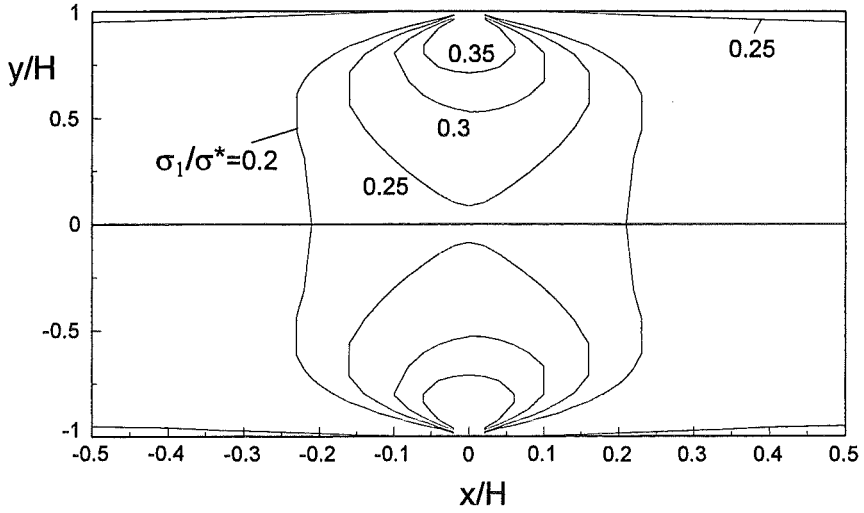

Fig. A4 Curves of constant first principal stress σ_1.

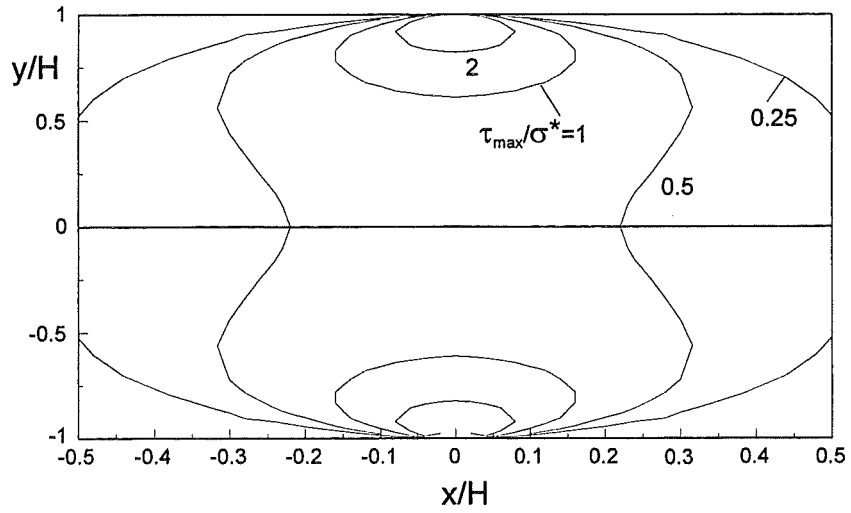

Fig. A5 Curves of constant maximum shear stress τ_{max}.